Cell

Regulation of Ferroptotic Cancer Cell Death by GPX4

Wan Seok Yang,[1,8] Rohitha SriRamaratnam,[2,8] Matthew E. Welsch,[2] Kenichi Shimada,[1] Rachid Skouta,[1]
Vasanthi S. Viswanathan,[1,4] Jaime H. Cheah,[4] Paul A. Clemons,[4] Alykhan F. Shamji,[4] Clary B. Clish,[4] Lewis M. Brown,[1,6]
Albert W. Girotti,[5] Virginia W. Cornish,[2] Stuart L. Schreiber,[4] and Brent R. Stockwell[1,2,3,7,*]
[1]Department of Biological Sciences, Columbia University, 1208 Northwest Corner Building, 12th Floor, 550 West 120th Street, MC 4846, New York, NY 10027, USA
[2]Department of Chemistry, Columbia University, 1208 Northwest Corner Building, 12th Floor, 550 West 120th Street, MC 4846, New York, NY 10027, USA
[3]Howard Hughes Medical Institute, Columbia University, 1208 Northwest Corner Building, 12th Floor, 550 West 120th Street, MC 4846, New York, NY 10027, USA
[4]Broad Institute of Harvard and MIT, Cambridge, MA 02142, USA
[5]Department of Biochemistry, Medical College of Wisconsin, Milwaukee, WI 53226, USA
[6]Quantitative Proteomics Center, Columbia University, New York, NY 10027, USA
[7]Department of Systems Biology, Columbia University Medical Center, New York, NY 10032, USA
[8]These authors contributed equally to this work
*Correspondence: bstockwell@columbia.edu

http://dx.doi.org/10.1016/j.cell.2013.12.010

SUMMARY

Ferroptosis is a form of nonapoptotic cell death for which key regulators remain unknown. We sought a common mediator for the lethality of 12 ferroptosis-inducing small molecules. We used targeted metabolomic profiling to discover that depletion of glutathione causes inactivation of glutathione peroxidases (GPXs) in response to one class of compounds and a chemoproteomics strategy to discover that GPX4 is directly inhibited by a second class of compounds. GPX4 overexpression and knockdown modulated the lethality of 12 ferroptosis inducers, but not of 11 compounds with other lethal mechanisms. In addition, two representative ferroptosis inducers prevented tumor growth in xenograft mouse tumor models. Sensitivity profiling in 177 cancer cell lines revealed that diffuse large B cell lymphomas and renal cell carcinomas are particularly susceptible to GPX4-regulated ferroptosis. Thus, GPX4 is an essential regulator of ferroptotic cancer cell death.

INTRODUCTION

Cells can undergo regulated forms of cell death in a variety of contexts (Galluzzi et al., 2012), including during development (Penaloza et al., 2006). Activation of alternative regulated cell death mechanisms may be beneficial for treating diseases such as cancer, in which apoptotic cell death mechanisms are suppressed due to genetic alterations. Indeed, activation of alternative cell death pathways may overcome the drug resistance associated with existing chemotherapeutic agents, providing new drug targets.

Regulators of apoptosis have been targeted with small molecules to induce cell death in cancer cells (Cotter, 2009). Recently, regulated, nonapoptotic cell death processes have been discovered, including necroptosis (Degterev et al., 2005) and ferroptosis (Dixon et al., 2012).

Ferroptosis is a mode of cell death involving the production of iron-dependent reactive oxygen species (ROS). In engineered human fibroblast cell lines, the small molecule erastin was found to induce preferential lethality in cells overexpressing oncogenic HRAS (Dolma et al., 2003). Erastin-induced ferroptotic cell death was distinct from apoptosis, necrosis, and autophagy, based on morphological, biochemical, and genetic criteria. Ferroptosis involves metabolic dysfunction that results in the production of both cytosolic and lipid ROS, independent of mitochondria but dependent on NADPH oxidases in some cell contexts (Dixon et al., 2012).

We have reported the identification of additional small molecules, named RSL3 (Yang and Stockwell, 2008a), ML162, and DPI10 (Weïwer et al., 2012), that display oncogenic-RAS-synthetic-lethality (the RSL phenotype) in engineered fibroblast-derived tumorigenic cell lines. Here, we sought to test whether these and other compounds also induce ferroptosis, and whether they could be used to elucidate a central regulator of ferroptosis, which controls cell death by all FIN (*f*erroptosis *in*ducing) compounds.

We focused initially on erastin and RSL3. Erastin reprograms cancer cell metabolism by modulating VDAC2/VDAC3 (Yagoda et al., 2007) and system x_c^- (Dixon et al., 2012) to trigger ferroptosis, whereas RSL3-induced ferroptosis is not dependent on these factors (Yang and Stockwell, 2008a) but results in a similar downstream cell death phenotype. Thus, we viewed erastin and RSL3 as ideal probes to elucidate conserved downstream regulators of ferroptosis. We used metabolomic profiling to evaluate comprehensively changes in metabolism occurring upon erastin treatment, and chemoproteomics to identify candidate target proteins for RSL3, which led to the discovery of a common pathway regulating cell death in response to all known compounds that induce ferroptosis.

RESULTS

Erastin Depletes Glutathione to Trigger Selective Ferroptosis

To investigate the global changes in metabolism induced by erastin, we treated HT-1080 fibrosarcoma cells with DMSO or erastin, and extracted polar and lipid metabolites. The metabolite extract was subjected to liquid chromatography-tandem mass spectrometry (LC-MS/MS) analysis to determine the quantity 149 polar and 115 lipid metabolites (Table S1 available online; Figure 1A). Both reduced glutathione (GSH) and oxidized glutathione (GSSG) were depleted significantly upon erastin treatment, whereas the level of lysophosphatidyl cholines (lysoPCs) was increased; the increase in lysoPCs may reflect the generation of lipid ROS during erastin-induced ferroptosis because PCs have been found to be converted to lysoPCs (deacylated PCs) upon lipid oxidation (Parthasarathy et al., 1985).

The significant depletion of GSH/GSSG was consistent with the fact that erastin induces the formation of ROS, causing an oxidative cell death. GSH/GSSG constitutes a major cellular antioxidant system and provides reducing equivalents to eliminate oxidative species. We treated three cell lines with erastin, determined GSH levels using Ellman's reagent, and confirmed the dose-dependent, GSH-depleting effect of erastin (Figures 1B and S1A). We found that GSH depletion by erastin is necessary for erastin's lethality because supplementing the culture medium with GSH or N-acetylcysteine (NAC), a biosynthetic precursor to GSH, prevented erastin-induced cell death (Figure S1B).

We sought to test further whether the glutathione-depleting activity of erastin was essential for lethality. We established a synthetic route to create six erastin analogs (see Data S1 for synthesis) and tested these analogs for selective lethality in BJ-derived engineered cell lines (Figure 1C). Three compounds (MEII, PE, and AE) retained selective lethality, whereas three compounds (A8, PYR, and dMK) were not lethal (Figure 1C). Lethal analogs of erastin depleted cellular GSH more effectively than nonlethal analogs of erastin (Figure 1D), which further suggested that the GSH-depleting activity of erastin is necessary for erastin lethality.

We reasoned that, if GSH depletion was contributing to erastin's lethality, then GSH depletion by other reagents might partially mimic erastin's selective lethality in the BJ-cell line system, which consists of isogenic cell lines (two with and two without oncogenic HRAS), through which ferroptosis-inducing compounds such as erastin were discovered. When the four BJ-derived cells were treated with BSO, an oncogenic HRAS-selective lethal phenotype was observed under conditions of low cell density (Figure 1E), suggesting that GSH depletion is sufficient for induction of ferroptosis in BJ cells with oncogenic HRAS overexpression, although additional factors may enhance the potency and efficacy of the lethality caused by GSH depletion under more general circumstances. These results indicated that erastin depletes GSH through preventing cystine uptake via inhibition of system x_c^- (Dixon et al., 2012).

Erastin Inactivates GPX Enzymes through GSH Depletion

Given that we found GSH depletion to be critical for erastin-induced ferroptosis, we investigated how GSH depletion by erastin was able to induce selective lethality in the engineered BJ cell lines. It has been hypothesized that most cancer cells, including RAS-transformed fibroblasts (Irani et al., 1997), are under high levels of oxidative stress (Szatrowski and Nathan, 1991), which therefore needs to be counteracted by increasing the ROS-scavenging capacity, to prevent oxidative damage (Hussain et al., 2003). In this model, targeting ROS-scavenging systems through multiple points, including GSH depletion, would cause an imbalance in this equilibrium, leading to oxidative cell death (Trachootham et al., 2006). In order to test whether this simple hypothesis could explain erastin's selective lethality, we examined basal ROS levels in the BJ-derived engineered cell lines using H_2DCF, a cytosolic ROS sensor, and confirmed that BJeLR cells have modestly elevated ROS levels compared to BJeH (BJ-TERT) and BJeHLT (BJ-TERT/LT/ST) cells (Figure 2A). We then treated the four BJ-derived cell lines with an SOD inhibitor (DETC), a thiol-reactive reagent (DIA), a thioredoxin reductase inhibitor (DCNB), or a catalase inhibitor (ATZ) (Figures 2B and S2). Three of these antioxidant inhibitors (DETC, DIA, and DCNB) killed BJ-derived cells, but they neither depleted GSH nor displayed selective lethality, which was in contrast to the two GSH-depleting reagents, erastin and BSO (Figures 2B, 2C, and S2). The results indicate that it is not possible to induce selective ferroptosis in the BJ-derived cell lines by simply targeting the antioxidant network. Instead, unique biochemical and metabolic changes downstream of GSH depletion were likely to be responsible for the selective induction of ferroptosis.

The degree of GSH depletion upon erastin treatment in the four BJ cell lines was also examined (Figure 2D). We found that these four BJ-derived cell lines contained varying amounts of basal GSH in the absence of any treatment, as reported previously by Kang and Enger (1992), but were depleted of GSH to a similar extent upon erastin treatment. The concentration of erastin used in this experiment (10 μM) was lethal to BJeLR and DRD cells (expressing $HRAS^{V12}$) but was not lethal to BJeH and BJeHLT cells (with wild-type RAS), even upon prolonged incubation (Figure 2B). Therefore, the selective lethality among these cell lines was not caused by differential depletion of GSH or by differences in the basal level of GSH.

We then treated BJeLR cells with either GSH-depleting reagents (erastin or BSO) or other antioxidant-targeting reagents (DETC, DIA, and DCNB), and stained cells with either BODIPY-C11, a membrane-targeted lipid ROS sensor, or H_2DCF, a cytoplasmic ROS sensor, to detect changes in ROS accumulation upon compound treatment (Figure 2E). GSH-depleting reagents strongly increased BODIPY-C11 and H_2DCF signals, whereas other antioxidant inhibitors did not increase the fluorescence signals from either ROS sensor, indicating that both cytosolic and lipid ROS levels were increased selectively by GSH depletion in the oncogenic HRAS-containing cell lines (Figure 2E).

We considered that one consequence of GSH depletion could be inactivation of glutathione-dependent peroxidases (GPXs).

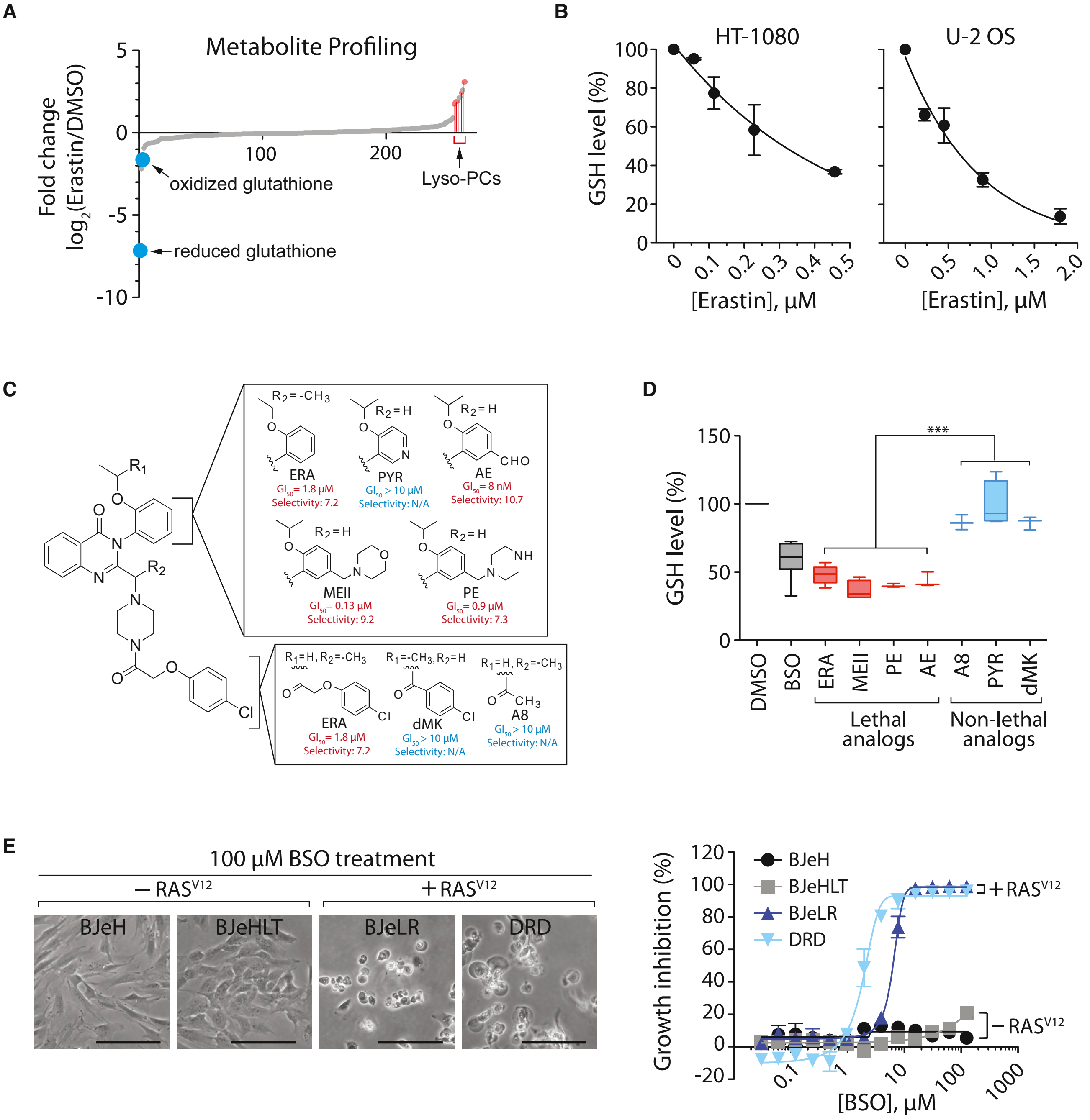

Figure 1. Ferroptosis Involves Generation of Lyso-PC and Depletion of Glutathione

(A) Changes in metabolites upon erastin treatment.

(B) Dose-dependent depletion of GSH by erastin in HT-1080 cells and U-2 OS cells.

(C) Structure and activity of erastin (ERA) analogs. Potency (GI$_{50}$; concentration required for 50% growth inhibition) and selectivity (ratio of GI$_{50}$ in HRAS wild-type cells divided by GI$_{50}$ in HRAS mutant cells) of each analog are shown. PYR, pyridine erastin; AE, aldehyde erastin; MEII, morpholine erastin II; PE, piperazine erastin.

(D) GSH depletion by erastin analogs. HT-1080 cells were incubated with 10 μM erastin analogs for 5 hr or 100 μM BSO for 12 hr. BSO was used as a positive control for GSH depletion. Data were normalized to the DMSO sample. Box-and-whisker plots (n = 3–8) are as follows: midline represents median, box is the 25th–75th percentiles, and whiskers are minimum and maximum. ***$p < 0.001$.

(E) BSO induces selective lethality in BJ-derived tumorigenic cells expressing oncogenic HRAS. Scale bars, 60 μm.

In (B) and (E), data are presented as mean ± SD (n = 3). See also Figure S1 and Table S1.

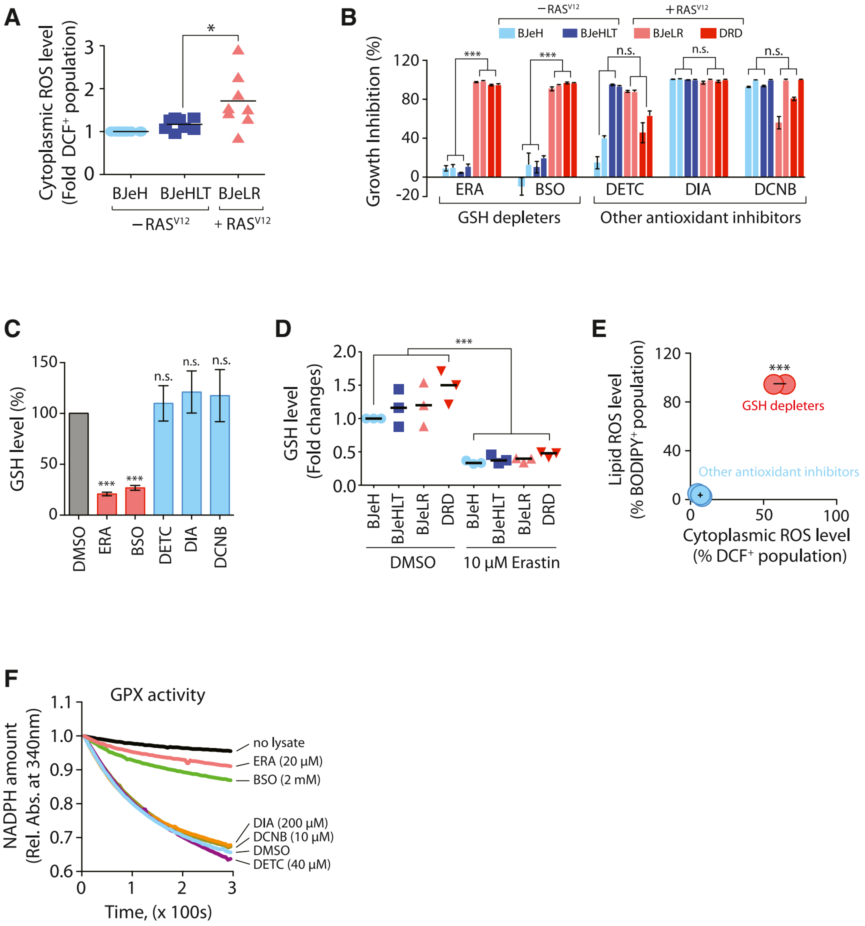

Figure 2. GSH Depletion Inactivates GPX Enzymes to Induce Ferroptosis

(A) Basal ROS levels among BJ-derived cell lines were compared (n = 8).

(B) The growth inhibition effect of antioxidant-targeting compounds was determined in the four BJ-derived cells (n = 3). The bar graph indicates growth inhibition at two different concentrations (2× GI_{50} and 4× GI_{50} for each compound in BJeLR cells).

(C) Other antioxidant inhibitors do not deplete GSH during cell death (n = 3).

(D) Erastin depletes cellular GSH equally in the four BJ-derived cell lines.

(E) GSH-depleting reagents elevated both cytosolic and lipid ROS level, whereas other antioxidant inhibitors did not (n = 3).

(F) GSH-depleting reagents (ERA and BSO) inhibited GPX activity. Rel. Abs., relative absorbance.

n.s., not significant; $^{*}p < 0.05$; $^{***}p < 0.001$. Error bars in (B), (C), and (E) represent mean ± SD. See also Figure S2.

GPXs catalyze the reduction of hydrogen peroxide and organic hydroperoxides to water or the corresponding alcohols, using GSH as an essential cofactor (Brigelius-Flohé and Maiorino, 2013).

The total activity of GPXs in BJeLR cells was examined using *tert*-butylhydroperoxide (tBuOOH) as a substrate, by monitoring the rate of NADPH oxidation, which is coupled to the tBuOOH-reducing activity of GPXs in cell lysates. When BJeLR cell lysates treated with vehicle only (0.08% DMSO) were added to the GPX activity assay, we observed a decrease in the amount of NADPH, indicating that tBuOOH was reduced by GPXs in the cell lysate (Figure 2F). Treatment of BJeLR cells with antioxidant inhibitors (DETC, DIA, and DCNB) did not affect GPX activity because the rate of NADPH oxidation was similar to the vehicle-only-treated sample.

When lysates from BJeLR cells that had been treated with GSH-depleting reagents (erastin or BSO) were analyzed, NADPH oxidation was prevented, indicating that GPXs were inactivated upon GSH depletion (Figure 2F). Taken together, these data indicate that erastin and BSO inactivate cellular GPXs, leading to the generation of cytoplasmic and lipid ROS. Other antioxidant inhibitors did not deplete GSH, an essential cofactor for GPX enzyme activity, and therefore, did not inhibit GPX activity and did not cause accumulation of peroxides.

RSL3 Binds to and Inactivates GPX4

Having determined that erastin acts by depleting GSH and inhibiting GPXs, we examined the mechanism of action of RSL3, another ferroptosis inducer (Yang and Stockwell, 2008a). Cell death induced by erastin and RSL3 shared common ferroptotic features, such as iron, MEK, and ROS dependence; however, RSL3 was not dependent on VDAC2/VDAC3 or system x_c^- implying that a different initiating mechanism could converge on a similar form of ferroptotic cell death. We thus used RSL3 as a probe to illuminate the shared downstream mechanism involved in executing ferroptosis.

When we examined cellular GSH levels during RSL3-induced cell death, we found that GSH remained unaffected by a lethal RSL3 concentration (2 μM) in BJeLR cells, which was in contrast to erastin's effect (Figure 3A). However, BODIPY-C11 staining revealed the generation of lipid ROS in RSL3-treated BJeLR cells, which indicated that lipid oxidation is common to both erastin-induced and RSL3-induced ferroptotic cell death (Figure 3B).

In order to understand the mechanistic basis of RSL3's enigmatic induction of lipid ROS in the absence of GSH depletion, we used affinity-based chemoproteomics to identify candidate target proteins for RSL3. We discovered that the chloroacetamide moiety of RSL3 was essential for its activity and that replacement with other electrophiles resulted in a loss of potency (Table S2; see Data S1 for synthesis). These data suggested that RSL3 targets an enzyme with a nucleophilic active site, such as serine, threonine, cysteine, or selenocysteine. Despite the potential for promiscuous reactivity of the chloroacetamide, we discovered that only the (1*S*, 3*R*)-RSL3 diastereomer of RSL3 exhibited selective lethality in the BJ cell system, whereas the three

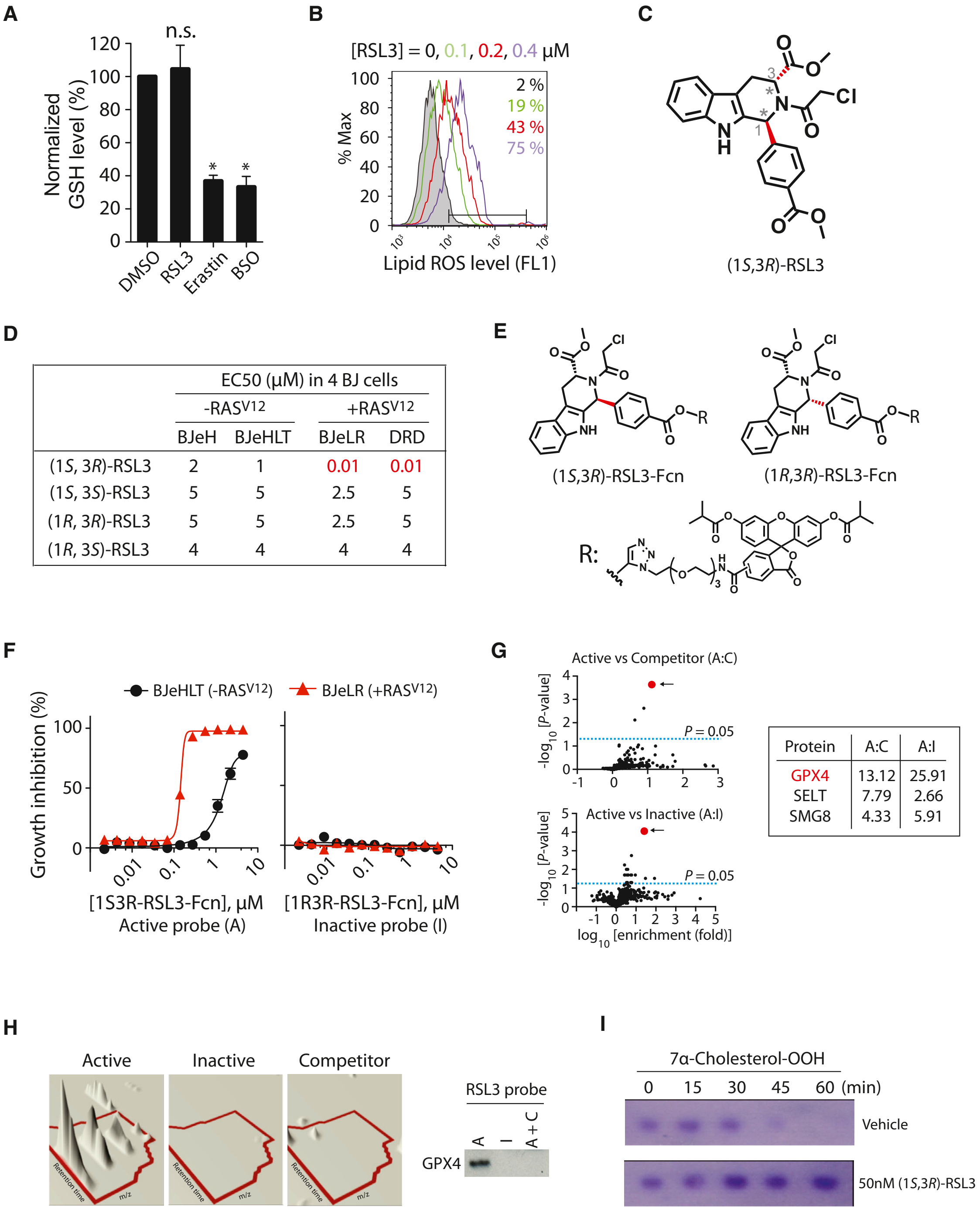

	EC50 (μM) in 4 BJ cells			
	$-RAS^{V12}$		$+RAS^{V12}$	
	BJeH	BJeHLT	BJeLR	DRD
(1*S*, 3*R*)-RSL3	2	1	0.01	0.01
(1*S*, 3*S*)-RSL3	5	5	2.5	5
(1*R*, 3*R*)-RSL3	5	5	2.5	5
(1*R*, 3*S*)-RSL3	4	4	4	4

Protein	A:C	A:I
GPX4	13.12	25.91
SELT	7.79	2.66
SMG8	4.33	5.91

Figure 3. RSL3 Binds to and Inhibits GPX4

(A) RSL3 does not deplete GSH. The level of GSH was determined after treating with 2 μM RSL3, 10 μM erastin, or 1 mM BSO (n = 3; $^*p < 0.05$). Error bars indicate ± SD.

(B) RSL3 treatment increased lipid ROS level, as erastin did.

(C) The structure of (1*S*, 3*R*)-RSL3 is shown.

(D) Only the (1*S*, 3*R*) diastereomer displayed selective lethality in $HRAS^{V12}$-expressing cells in the four BJ-derived cell lines.

(E) Structure of RSL3 affinity probes used in the chemoproteomics experiments is shown. Fcn, fluorescein affinity tag.

(F) The active affinity probe with the (1*S*, 3*R*) stereochemistry exhibited selective lethality against cells with $HRAS^{V12}$, whereas an affinity probe with the (1*R*, 3*R*) stereochemistry was not lethal.

(legend continued on next page)

other diastereomers of RSL3 lacked selectivity and were more than 100-fold less potent (Figures 3C and 3D; Table S2; Data S1 for synthesis). These results suggested that (1*S*, 3*R*)-RSL3 covalently binds to one or more proteins to induce the potent and selective lethality observed in BJ cells expressing HRAS^{V12}.

Affinity reagents were synthesized by attaching an isobutyryl-protected fluorescein tag via a polyethylene glycol (PEG) linker to the phenyl substituent at the 1 position in the tetrahydro-β-carboline ring system of RSL3, which was found to tolerate structural modifications. Despite a loss in potency upon incorporation of the affinity tag, 10-fold oncogenic HRAS selectivity was retained for an affinity analog with the active (1*S*, 3*R*) stereochemistry, whereas an affinity analog with the (1*R*, 3*R*) stereochemistry showed no activity (Figures 3E and 3F; see Data S1 for synthesis).

Samples for proteomic analysis were prepared by treating intact BJeLR cells with (1*S*, 3*R*)-RSL3-fluorescein (active probe treatment), (1*R*, 3*R*)-RSL3-fluorescein (inactive probe treatment), or (1*S*, 3*R*)-RSL3-fluorescein pretreated with free (1*S*, 3*R*)-RSL3 (competitor treatment). Treated cells were lysed, and fluorescein-tagged proteins were affinity purified using Sepharose beads coupled to an anti-fluorescein antibody. Eluted proteins were identified with a Synapt G2 HDMS mass spectrometer (Waters) using a quantitative label-free shotgun proteomic strategy with data-independent scanning (MS^E) and ion mobility spectrometry (see Extended Experimental Procedures).

Proteins enriched in “active probe” versus “inactive probe” and “active probe” versus “competitor” treatments were determined (Figure 3G). Three independent affinity preparations of each of these treatments were further subsampled in three LC-MS/MS analyses (Table S2). Candidates were chosen on the basis of (1) exhibiting enrichment in both active:inactive and active:competitor comparisons with $p < 0.01$ (with false discovery rate correction; see Extended Experimental Procedures) and (2) identification and quantitation by $n > 2$ tryptic peptides. This analysis ranked GPX4 (glutathione peroxidase 4, PhGPx) as the top candidate protein target for (1*S*, 3*R*)-RSL3 (Figure 3G; Table S2).

It was intriguing that GPX4 was identified as the most highly ranked candidate in our unbiased chemoproteomic approach to find target proteins for RSL3 because erastin inhibited cellular GPX enzymes through GSH depletion (Figures 1 and 2). We confirmed that GPX4 was purified specifically by the affinity analog (1*S*, 3*R*)-RSL3-fluorescein, using fresh samples prepared from BJeLR cells treated with the active probe, the inactive probe, or the competitor as before, analyzed for GPX4 abundance by western blot (Figures 3H and S3A).

In order to examine whether RSL3 binding to GPX4 inactivates the peroxidase activity of GPX4, we treated a clone of the COH-BR1 breast cancer cell line overexpressing GPX4 (L7G4), with (1*S*, 3*R*)-RSL3 or vehicle only, prepared cell lysates, and incubated them with 7α-cholesterol hydroperoxide (7α-cholesterol-OOH) to determine the rate of reduction to the corresponding alcohol (7α-cholesterol-OH). 7α-cholesterol-OOH is a specific substrate for GPX4; no other GPX enzyme can catalyze the reduction of 7α-cholesterol-OOH (Kriska and Girotti, 2005). In vehicle-treated samples, 7α-cholesterol-OOH decreased over time in a GSH-dependent manner, due to reduction by GPX4 in the lysate. Upon treatment with (1*S*, 3*R*)-RSL3, however, no reduction of 7α-cholesterol-OOH was observed, indicating that GPX4 was inhibited by (1*S*, 3*R*)-RSL3 (Figure 3I; see Figure S3B for quantitation data). Treatment with the inactive diastereomer (1*R*, 3*R*)-RSL3 did not inhibit GPX4 activity (Figure S3C).

We used another proteomics data analysis tool, Elucidator (Rosetta Biosoftware), and found that only GPX4 was a significantly enriched protein common to both TransOmics and Elucidator analysis algorithms (Figure S3D). Evaluation of other candidates using specific siRNAs and shRNAs failed to show either modulation of (1*S*, 3*R*)-RSL3 sensitivity or cell killing (Figures S3E–S3I), which excludes the functional role of these other binding proteins on ferroptosis induced by (1*S*, 3*R*)-RSL3.

RNAi-Mediated GPX4 Knockdown Induces Ferroptosis

We hypothesized that, if RSL3 were to inhibit a protein essential for cancer cell viability, then reducing the levels of this protein would sensitize cells to RSL3. Silencing of GPX4 mRNA using shRNAs that cause partial knockdown of GPX4 strongly sensitized cells to (1*S*, 3*R*)-RSL3 (Figure 4A). Conversely, when we overexpressed GPX4, we found that it caused strong resistance to (1*S*, 3*R*)-RSL3 lethality (Figure 4B), as expected for a relevant target protein.

We were able to achieve a more effective knockdown of GPX4 using a pool of siRNAs targeting GPX4 (20-fold decrease in the GPX4 mRNA; Figure S4A) compared to a single clone of shRNA (5-fold decrease in the GPX4 mRNA; Figure 4A). With this more effective knockdown, HT-1080 cells underwent cell death with accompanying lipid ROS generation (Figure 4C). Cell death induced by siGPX4 was rescued by the same suppressors of RSL3—an iron chelator (DFOM), a MEK inhibitor (U0126), and an antioxidant (vitamin E [Vit. E])—which suggested that *GPX4* knockdown induced ferroptotic cell death (Figure 4D) similar to RSL3. None of these ferroptosis inhibitors suppressed cell death induced by siDeath, a control siRNA pool targeting multiple essential genes, highlighting the ferroptosis-specific action of these inhibitors (Figure 4D). Furthermore, siGPX4 induced selective cell death in BJeLR and DRD cells (with HRAS^{V12}), but not BJeH and BJeHLT cells (wild-type HRAS), which recapitulated the selective lethality of erastin and RSL3 (Figures 4E and

(G) Affinity-based chemoproteomics identified GPX4 (red dot) as the most likely binding protein for (1*S*, 3*R*)-RSL3. Fold enrichment values of peptides at the indicated condition and their FDR-adjusted p values were represented as volcano plots. The top three candidates are shown.

(H) Confirmation of GPX4 binding to active (1S, 3R)-RSL3 affinity probe. Left panel is a 3D visualization of isotopic clusters of peptide ILAFPCNQFGK from GPX4 as rendered by TransOmics software. Right panel: cell lysates prepared from BJeLR cells treated with active probe (A), inactive probe (I), or active probe in the presence of competitor (A+C) that were affinity purified by α-fluorescein antibodies. Then, the purified protein samples were probed for GPX4 by western blot using GPX4-specific antibody.

(I) (1*S*, 3*R*)-RSL3 inhibits enzyme activity of GPX4.

See also Figure S3 and Table S2.

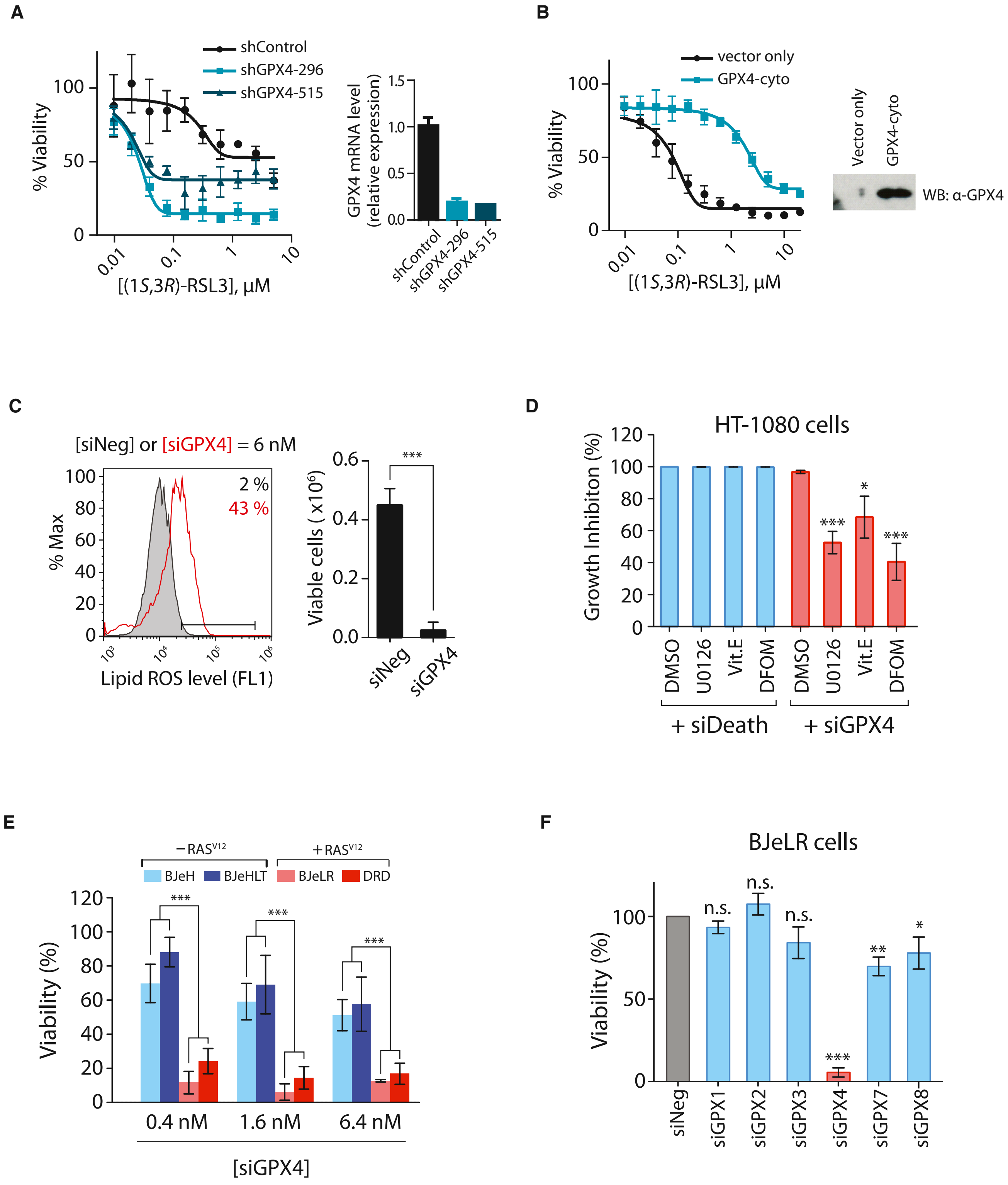

Figure 4. RSL3 Targets GPX4 to Induce Ferroptosis

(A) Knockdown of GPX4 using shRNAs rendered HT-1080 cells hypersensitive to (1*S*, 3*R*)-RSL3 lethality.

(B) Overexpression of GPX4 rendered HT-1080 cells resistant to (1*S*, 3*R*)-RSL3 lethality.

(C) HT-1080 cells transfected with a pool of siRNAs targeting GPX4 showed increased lipid ROS level as assessed by BODIPY-C11 staining. siNeg has no homology to any known mammalian genes and was used as a negative control.

(legend continued on next page)

S4B). These data suggested that GPX4 is the primary target of RSL3, mediating its ability to induce ferroptosis specifically in the oncogenic HRAS-containing BJ-derived fibroblasts.

There are eight isoforms of GPXs in humans with different tissue expression and substrate specificities. In BJeLR cells, six GPX isoforms are expressed (GPX1, GPX2, GPX3, GPX4, GPX7, and GPX8) as determined by RT-qPCR (Figure S4C). Knockdown of each isoform affected cell viability to varying levels; however, GPX4 knockdown was the most lethal to BJeLR cells, which highlights the prominent role of GPX4 inhibition in inducing cell death, as compared to other GPX enzymes (Figures 4F and S4D).

Taken together, these data suggest that GPX4 is a central regulator of ferroptosis induced by erastin and RSL3. Cell death was enhanced in the BJ-derived cell lines expressing HRAS^{V12} due to the increased basal ROS (Figure 2A) and enhanced lipid peroxidation after GPX4 inhibition, which caused selective lethality in this engineered isogenic cell line model.

GPX4 Regulates Ferroptosis Induced by 12 Divergent Compounds

In a larger screening campaign to find additional FIN compounds, 14 candidate compounds were discovered out of more than a million tested (Figure 5A; see Figure S5 for structures) (Weïwer et al., 2012; Yang et al., 2012). These 14 compounds displayed selective lethality in HRAS^{V12}-expressing cells in the four BJ-derived cell lines (Figure 5A; Table S3). We defined ten structurally diverse FIN groups, not including erastin or RSL3 (Figure 5A), to use in subsequent experiments.

BJeLR cells treated with each of the ten additional FIN compounds exhibited an increase in BODIPY-C11 fluorescence, indicating that lipid ROS were generated (Table S3 for individual flow cytometry data). We then tested 11 non-FIN compounds acting through diverse lethal mechanisms to see whether they induced lipid ROS generation using this assay (Table S3 for more information of 11 non-FIN compounds). These 11 diverse lethal compounds were confirmed to lack selective lethality in the four BJ-derived cell lines previously (Root et al., 2003), which suggested that they are not ferroptosis inducers. We found that 10 out of 11 of the non-FIN compounds did not generate lipid ROS, implying a specificity of lipid ROS generation for FIN compound-treated cells (Table S3 for individual flow cytometry data). It is likely that the reported ROS-generating activity of phenylarsine oxide was responsible for the oxidation of the BODIPY-C11 dye (Fanélus and Desrosiers, 2008).

In order to determine whether these FIN compounds genuinely induced ferroptosis, the functional requirement of lipid ROS during ferroptosis was examined by treating BJeLR cells with each lethal compound (FINs and non-FINs) in the presence of a lipophilic antioxidant, butylated hydroxytoluene (BHT). BHT strongly suppressed cell death induced by all FIN compounds (Table S3 for individual growth inhibition curves). The rescuing effect of BHT was specific to FIN compounds because BHT was not able to suppress cell death induced by 12 non-FIN compounds (Table S3 for individual growth inhibition curves). We quantified the degree of cell death suppression by calculating the normalized differences in the AUC (*a*rea *u*nder the concentration-response *c*urve) of the compound alone and that of the compound with BHT. Combined with the BODIPY-C11 staining data, these results revealed that the FIN compounds are mechanistically distinct from the 11 non-FIN compounds (Figure 5B). An extended death mechanism analysis using the modulatory profiling approach (Wolpaw et al., 2011) with four selected FIN compounds (erastin, PE, DPI2, and DPI10) revealed that they induced a similar form of cell death that was distinct from non-FIN compounds (Figure 5C). Taken together, these data indicate that compounds that display the RSL phenotype in the four-BJ cell system are ferroptosis inducers. These data also suggest that ferroptotic cell death is not limited to erastin and RSL3 but that a number of additional small molecules can be identified that induce ferroptosis, suggesting that it may be a more generally important mechanism of lethality.

In order to determine the generality of ferroptosis regulation by GPX4, we treated HT-1080 cells with each lethal compound (FIN compound or non-FIN compound) under a GPX4-inhibited condition (using BSO treatment, which depletes glutathione and therefore inhibits all GPXs), or a GPX4-upregulated condition (by overexpressing GPX4). GPX4 inhibition using BSO enhanced ferroptotic cell death induced by all FIN compounds, whereas GPX4 overexpression suppressed ferroptosis induced by all FIN compounds (Figure 5D and Table S3). The modulation effect of BSO and GPX4 overexpression was specific to FIN compounds because their effects on cell death induced by 11 non-FIN compounds were minimal (Figure 5D).

We speculated that these additional FIN compounds acted through mechanisms similar to those induced by erastin or RSL3; we examined whether these FIN compounds inhibited GPX4 in BJeLR cells. For a side-by-side comparison of GPX4 activity in multiple samples, we used an LC-MS-based GPX4 assay in which the GPX4 enzyme activity in cell lysates was measured by their capacity to reduce exogenously added phosphatidylcholine hydroperoxide (PC-OOH), a GPX4-specific substrate. When GPX4 was inhibited, cells could not reduce PC-OOH, which resulted in a signal for the $[\text{PC-OOH} + \text{H}]^+$ ion (m/z, 790.6) in the mass chromatogram. BJeLR cells treated with any of the eight FIN compounds (DPI7, DPI10, DPI12, DPI13, DPI17, DPI18, DPI19, and RSL3) lacked GPX4 activity, being unable to reduce exogenous PC-OOH (Figure 5E). On the other hand, a control non-FIN compound, staurosporine, and two known FIN compounds, erastin and DPI2, did not inhibit GPX4 activity in

---

(D) Known inhibitors of ferroptosis, 10 μM U0126, 100 μM Vit. E, or 100 μM DFOM, were able to suppress siGPX4-induced cell death, whereas they could not suppress cell death induced by siDeath.

(E) Knockdown of GPX4 displayed selective lethality in the four BJ-derived isogenic cell lines.

(F) Other GPX isoforms are not relevant to ferroptotic cell death.

The values in (D)–(F) were normalized to control samples transfected with siNeg. Bar graphs in (C)–(F) are mean ± SD (n = 3). $^*p < 0.05$; $^{**}p < 0.01$; $^{***}p < 0.001$. Data in (A) and (B) are presented as mean ± SD (n = 3).

See also Figure S4.

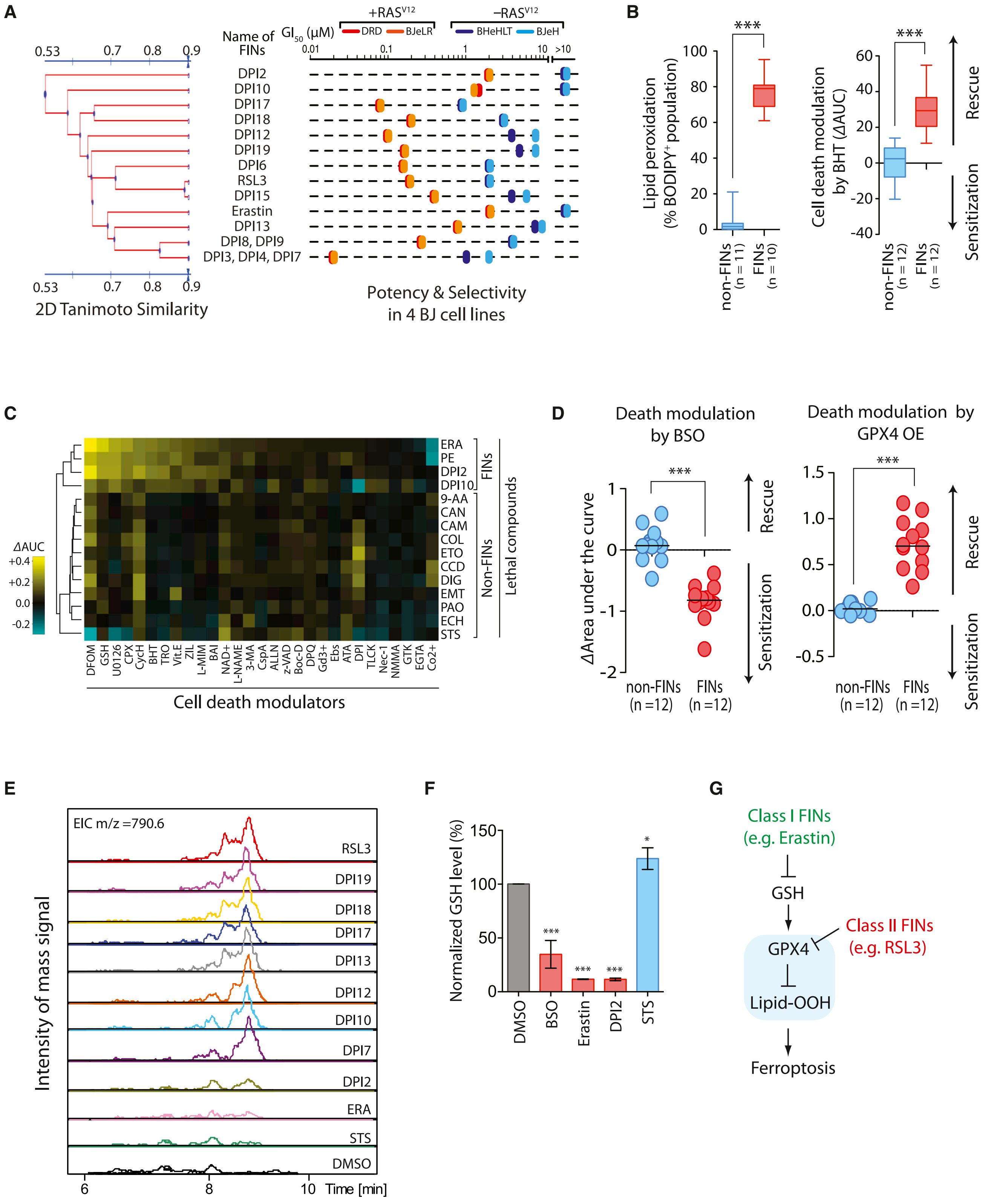

(legend on next page)

the assay. The LC-MS-based assay requires addition of exogenous GSH (5 mM) in the reaction mixture; therefore, it cannot detect indirect inhibitory effects on GPX4 by GSH-depleting agents such as BSO and erastin. We then determined the cellular GSH level in BJeLR cells treated with DPI2, the one FIN compound that did not inhibit GPX4 in the LC-MS-based assay, along with BSO and erastin as positive controls, and staurosporine as a negative control (Figure 5F). DPI2 depleted 90% of cellular GSH compared to untreated BJeLR cells, indicating that it acts through a mechanism similar to erastin to induce ferroptotic cell death (Figure 5F).

These results demonstrate that GPX4-regulated ferroptosis is a common mechanism shared by multiple independent small molecule scaffolds. All FIN compounds can be categorized into two classes based on the mode of GPX4 inhibition. One class, including erastin, inhibits GPX4 through GSH depletion. The second class inhibits GPX4 without GSH depletion, such as RSL3, which inhibits GPX4 directly (Figure 5G).

Ferroptosis Inducers Inhibit Tumor Growth in a Xenograft Mouse Model

We explored whether the GPX4-regulated ferroptotic cell death pathway could be utilized to suppress the growth of tumors in a xenograft mouse model. First, we searched for a pharmacodynamic marker associated with ferroptotic cell death. A set of 83 genes that were known to be perturbed upon oxidative stress was surveyed to determine whether the expression level of any gene was affected during ferroptosis induced by erastin or RSL3 (Figure 6A; Table S4). This analysis revealed that *PTGS2*, a gene encoding cyclooxygenase-2 (COX-2), was the most upregulated gene in BJeLR cells upon treatment with either erastin or (1*S*, 3*R*)-RSL3 (Figure 6A). The functional relevance of *PTGS2* on ferroptosis was examined using indomethacin, a PTGS-1/PTGS-2 (COX-1/COX-2) inhibitor. Ferroptotic cell death by erastin or (1*S*, 3*R*)-RSL3 was not affected by indomethacin treatment, suggesting that *PTGS2* upregulation is simply a downstream marker of ferroptosis (Figure S6A).

We also developed a more effective analog of erastin that could be tested in vivo. Erastin itself has modest water solubility and is metabolically labile, precluding its use in vivo. We discovered that introduction of a piperazine moiety into the aniline ring of erastin resulted in a more water-soluble and more metabolically stable compound that was suitable for in vivo experiments; we named this compound piperazine erastin (PE). PE upregulated *PTGS2* in BJeLR cells (Figure 6B). Cotreatment of Vit. E suppressed *PTGS2* induction by PE, which indicates that *PTGS2* upregulation is downstream of the lipid peroxidation that occurs during ferroptosis (Figure 6B). (1*S*, 3*R*)-RSL3, but not (1*R*, 3*R*)-RSL3, increased *PTGS2* expression (Figure 6B). In addition, knockdown of GPX4 using siRNAs markedly increased *PTGS2* mRNA abundance, whereas the effect on *PTGS2* mRNA abundance of siDeath was minimal (Figure 6B). Kumagai et al. (2004) reported upregulation of *PTGS2* by 4-HNE, an end product of oxidized lipids in an atherosclerosis model. Moreover, DNA microarray analysis of gene expression in skin tissue samples obtained from *Gpx4*-deficient mice identified *Ptgs2* as a key gene upregulated as a consequence of *Gpx4* loss (Sengupta et al., 2013). Taken together, these data confirm that *PTGS2* upregulation is a suitable marker for the lipid peroxidation that occurs during GPX4-regulated ferroptosis.

We tested whether (1*S*, 3*R*)-RSL3 could prevent tumor growth in athymic nude mice implanted with subcutaneous (s.c.) xenograft tumors derived from BJeLR cells. Mice were injected with BJeLR cells s.c. and then with 100 mg/kg (1*S*, 3*R*)-RSL3 in the same site 1 day later. The (1*S*, 3*R*)-RSL3 injection was repeated twice each week for 2 weeks. Three weeks later, we observed significant prevention of tumor growth in (1*S*, 3*R*)-RSL3-treated animals (Figure 6C; $p = 0.0053$). Subsequently, we examined the ability of (1*S*, 3*R*)-RSL3 to shrink preexisting tumors in a therapeutic study, using s.c. xenograft tumors that had been allowed to grow for 1 week and then treated with 100 mg/kg (1*S*, 3*R*)-RSL3 twice a week for 2 weeks. Again, we observed a significant reduction in tumor volume compared with the vehicle-treated control group, with this infrequent dosing (Figure 6C; $p = 0.038$). The inhibition of tumor growth was likely due to the induction of ferroptosis, as determined by *Ptgs2* upregulation in (1*S*, 3*R*)-RSL3-treated tumors (Figure 6C).

We then evaluated the erastin analog PE in a tumor-prevention model using nude mice into which HT-1080 cells, the human fibrosarcoma cell line, had been injected. As mentioned, PE has improved metabolic stability (Figure 6D) and water solubility (0.086 mM for erastin versus 1.4 mM for PE) compared to erastin. PE was affected similarly by cell death modulators as erastin and displayed a distinct pattern from other non-FIN lethal compounds, indicating that PE, like erastin, induces ferroptosis in HT-1080 cells (Figure 5C; Spearman correlation coefficient,

Figure 5. Ferroptosis Occurs through a GPX4-Regulated Pathway

(A) Discovery of additional FINs based on selective lethality in the four BJ cell lines.

(B) FINs (red) are distinct from non-FINs (blue) in accompanying lipid ROS generation during the cell death process and in death suppression by an antioxidant, BHT.

(C) Modulatory profiling (Wolpaw et al., 2011) with erastin, PE, DPI2, DPI10, and other lethal molecules confirmed that PE, DPI2, and DPI10 induced a similar form of cell death as erastin in HT-1080 cells. ΔAUC with a positive sign indicates suppression of cell death, whereas a negative sign indicates sensitization by cell death modulators upon lethal compound treatment.

(D) Inhibition of GPX4 by BSO sensitized cells to death induced by 12 FIN compounds, whereas activation of GPX4 by cDNA overexpression rescued cells from the lethality of FIN compounds.

(E) Eight structurally diverse FIN compounds inhibited GPX4, whereas two FIN compounds, DPI2 and erastin, and the negative control staurosporine (STS), a non-FIN compound, did not show direct GPX4 inhibition in this LC-MS-based assay.

(F) The two FIN compounds, DPI2 and erastin, depleted cellular GSH, which inhibits GPX4 indirectly, whereas staurosporine did not deplete GSH. Bar graph indicates mean ± SD (n = 3).

(G) Model of GPX4-regulated ferroptosis pathway. Ferroptosis inducers can be categorized into two classes based on the mode of GPX4 inhibition.

*$p < 0.05$; ***$p < 0.001$. See also Figure S5 and Table S3.

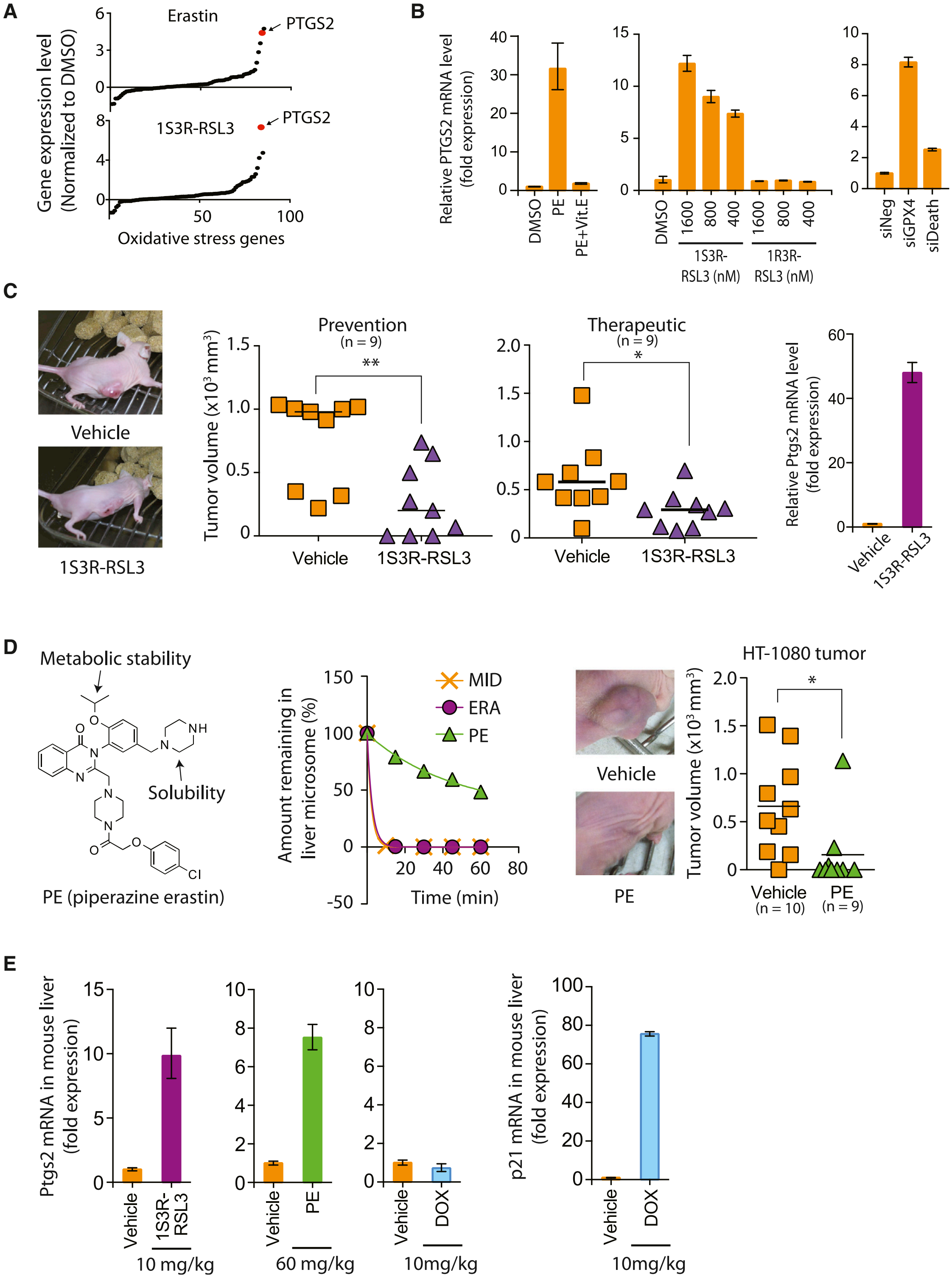

Figure 6. Ferroptosis Suppresses Tumor Growth in a Xenograft Mouse Model

(A) Upregulation of *PTGS2* expression upon erastin and (1*S*, 3*R*)-RSL3 treatments.

(B) *PTGS2* expression was induced by PE, (1*S*, 3*R*)-RSL3, and siGPX4, but not by PE with Vit. E, (1*R*, 3*R*)-RSL3, and siDeath.

(C) (1*S*, 3*R*)-RSL3 inhibited tumor formation and tumor progression through induction of ferroptosis as demonstrated by upregulation of *PTGS2* in the tumors. (1*S*, 3*R*)-RSL3 was administered s.c. twice a week for 2 weeks.

(legend continued on next page)

0.9291; $p < 0.0001$). HT-1080 cells were injected to the flank of athymic nude mice. One day later, vehicle or PE (40 mg/kg) was s.c. delivered to the nude mice with a twice-a-week schedule for 1 week. Then, vehicle or PE (30 mg/kg) was administered to the mice through tail vein once every other day for 6 days. We observed a significant delay in tumor growth in the PE-treated group compared to the vehicle-treated group (Figure 6D).

The systemic toxicity and pharmacodynamics of these two ferroptosis inducers, PE and (1*S*, 3*R*)-RSL3, were assessed by injecting the compounds through the tail vein at 60 and 10 mg/kg, respectively. At these doses, we observed upregulation of *Ptgs2* in mouse liver (Figure 6E). In contrast, tail vein injection of the chemotherapeutic agent doxorubicin did not show any induction of *Ptgs2* in the same tissue, confirming the specificity of *Ptgs2* as a pharmacodynamic marker (Figure 6E). As a control, we detected robust upregulation of the *p21* gene, a biomarker for p53 activation induced by doxorubicin-mediated DNA damage (Figure 6E). Regardless of ferroptosis activation in the liver, we observed no overt toxicity in either animal study, as assessed by the lack of acute lethality, and the lack of significant body weight reductions. Independently, NCI's DTP (developmental therapeutics program) evaluated in vivo the toxicity of intraperitoneal injection of (1*S*, 3*R*)-RSL3 and observed no toxicity up to 400 mg/kg dose, which suggested that these doses of (1*S*, 3*R*)-RSL3 were well tolerated (Figure S6).

Diffuse Large B Cell Lymphomas and Renal Cell Carcinomas Are Sensitive to Ferroptosis

We investigated whether the mutation status of *RAS* genes in cancer cells is a predictor of sensitivity to erastin-induced ferroptotic cell death, by testing erastin in 117 cancer cell lines from different tissues such as hematopoietic and lymphoid tissue, large intestine, lung, ovary, and skin (Table S5). The cancer cell line panel contained 38 cancer cell lines with oncogenic-RAS mutations, which allowed us to examine the correlation between RAS mutation status and erastin potency.

Although erastin displayed synthetic lethality in the engineered cells, it did not show selective lethality in *RAS*-mutated cancer cell lines over *RAS* wild-type counterparts (Figures S7A and S7B) in this large and diverse panel of cell lines. Although *RAS* mutations sensitize to ferroptosis in an individual genetic context, there are other more dominant determinants of sensitivity when analyzing sensitivity across diverse contexts. Analysis of the 117-cell line erastin sensitivity data revealed that diffuse large B cell lymphomas (DLBCLs) were particularly sensitive (Figure 7A). When we divided the 117 cell lines into sensitive and resistant groups based on AUC values (sensitive if AUC < 3.5, resistant if AUC > 5.5), DLBCLs were enriched in the sensitive group (Figure 7A, $p = 0.01$ by chi-square test; $p = 0.025$ by logistical regression analysis [Basu et al., 2013]). In a larger drug-screening analysis, it was observed that suspension cell lines were generally more sensitive to growth inhibitory effects of small molecules (Basu et al., 2013). In order to examine whether the observed sensitivity enrichment in our analysis was due to the general sensitivity of suspension cell lines, we tested erastin in seven DLBCL cell lines, five acute myeloid leukemia (AML) cell lines, and five multiple myeloma (MM) cell lines. The DLBCLs displayed increased sensitivity among these suspension cell lines, which suggested that DLBCLs are particularly sensitive to ferroptotic cell death (Figure 7B; see Figure S7C for individual concentration-dependent curve).

We further analyzed the sensitivity of DLBCLs and other hematopoietic cell lines against 203 diverse lethal compounds to see if DLBCLs are generally sensitive to lethal compounds (Figure 7C). DLBCL cell lines in fact displayed a slight resistance on average to all compounds tested compared to other hematopoietic cell lines ($p < 3 \times 10^{-4}$, Kolmogorov-Smirnov test). This indicates that the enhanced sensitivity of DLBCLs to erastin-induced ferroptosis is not due to a general sensitivity to all compounds.

We confirmed that erastin and RSL3 generated lipid peroxides in two DLBCL cell lines: SU-DHL-8 and WSU-DLCL-2 (Figure 7D). Moreover, erastin-induced cell death was rescued by a lipophilic antioxidant (Vit. E) in these cell lines, indicating that cells were dying through the lipid ROS characteristic of ferroptosis (Figure 7E).

The potency of erastin was also determined in a 60-cancer cell line panel (NCI60) (Shoemaker, 2006) from eight diverse tissues, which revealed increased sensitivity of renal cell carcinomas (RCCs), compared to the other tissues examined (Figures 7F and S7D). We confirmed the potency of erastin in these RCC cell lines and observed generation of lipid ROS in two representative RCC cell lines (Figures 7G and 7H). Moreover, erastin-induced death of these cell lines was suppressed by a lipophilic antioxidant (Vit. E) (Figure 7I). The two RCC cell lines expressed GPX4, as determined by western blot with a GPX4-specific antibody (Figure 7J). Knockdown of GPX4 using siRNAs decreased the level of GPX4 protein and was sufficient to kill these RCC cell lines (Figure 7J). Moreover, these cells died via a characteristic ferroptotic death upon GPX4 knockdown (Figure 7K).

DISCUSSION

Unlike other GPXs, GPX4 can catalyze the reduction of lipid peroxides in a complex cellular membrane environment (Brigelius-Flohé and Maiorino, 2013). Systemic deletion of *Gpx4* in mice causes embryonic lethality, which was not observed when other *Gpx* genes were deleted (Ran et al., 2004), suggesting a unique role for Gpx4 in physiology. Four groups independently created

(D) PE showed efficacy in preventing HT-1080 tumor formation in a mouse xenograft model. The left view shows the structure of PE. The middle view is a mouse liver microsome assay demonstrating improved metabolic stability of PE over erastin. Midazolam was used as a positive control for metabolic degradation. The right view shows images representative of tumors in live mice from each treatment group. PE was delivered s.c. twice a week for 1 week and then delivered through tail vein injection once every other day for 6 days.

(E) Pharmacodynamics of PE and (1*S*, 3*R*)-RSL3 in the mouse liver tissue.

Bar graphs in (B), (C), and (E) represent mean ± SD (n = 3). In (C) and (D), the lines in the tumor volume plots indicate mean of nine data points. *$p < 0.05$; **$p < 0.01$. See also Figure S6 and Table S4.

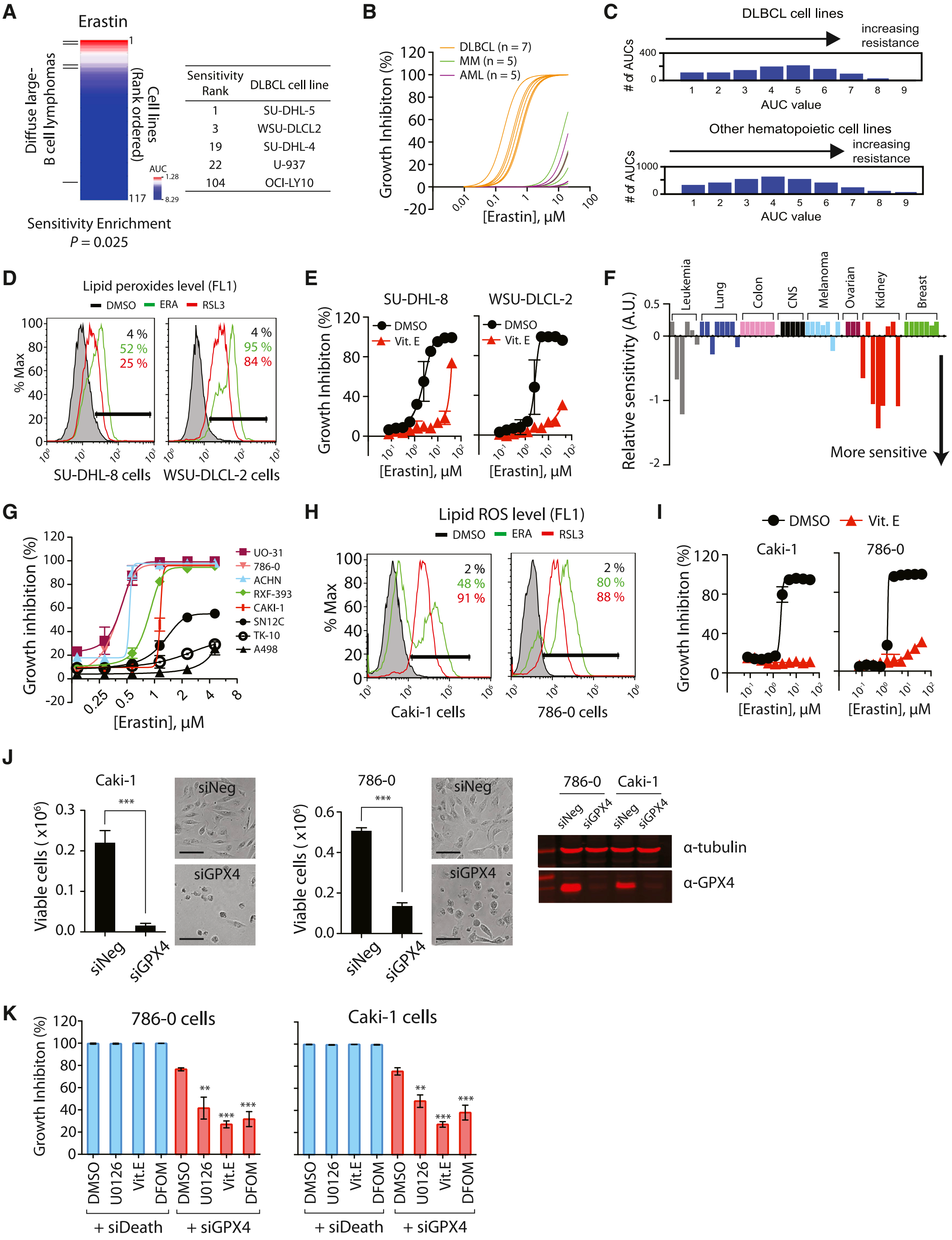

Figure 7. DLBCLs and RCCs Are Sensitive to GPX4-Regulated Ferroptosis

(A) Testing erastin in 117 cancer cell lines revealed DLBCLs as a cancer subtype susceptible to ferroptosis. DLBCL cell lines are marked with lines on the left. The table shows the name of DLBCL cell lines along with the sensitivity rank.

(B) DLBCLs were more sensitive to erastin than AML and MM cells.

(C) DLBCL cell lines are no more sensitive to lethal compounds than other hematopoietic cell lines. The total number of AUCs in the analysis was 3,883 (972 for DLBCL and 2,911 for other hematopoietic cell lines).

(D and E) DLBCL cells died through a mechanism characteristic of ferroptosis, as determined by lipid peroxide generation and death rescue by Vit. E.

(legend continued on next page)

conditional *Gpx4* knockout mice and analyzed the cell death mechanisms after *Gpx4* inhibition (Seiler et al., 2008; Sengupta et al., 2013; Ueta et al., 2012; Yoo et al., 2012). Lipid peroxidation was observed in all knockout models, highlighting the importance of Gpx4 for protecting cells from detrimental effects of lipid peroxides. Systemic deletion of *Gpx4* was lethal to mice partly due to the nervous system damage caused by neuronal loss (Seiler et al., 2008; Yoo et al., 2012).

In models in which *Gpx4* deletion caused lethality or cell loss, it is likely that ferroptosis had occurred. Indeed, mouse embryonic fibroblasts (MEFs) from conditional *Gpx4* knockout mice died with lipid peroxide generation upon *Gpx4* deletion. Supplementing Vit. E to these MEFs in culture rescued cell death (Seiler et al., 2008).

Elevation of lipid peroxidation upon GPX4 inhibition raises the question of the source of lipid peroxides in normal cellular physiology. Cellular iron may be the most important factor in lipid peroxide generation during ferroptosis. Indeed, iron chelators suppress ferroptosis (Yang and Stockwell, 2008a). Some oncogenes, including *RAS* and *MYC*, are known to alter iron metabolism by increasing iron abundance in cells and promoting transformation (Kakhlon et al., 2002; O'Donnell et al., 2006).

In summary, we have determined that Gpx4 is a central regulator of ferroptosis and that ferroptosis can be induced in mouse tumor xenografts, providing a possible therapeutic application of ferroptosis-inducing compounds. See the Extended Discussion for more information.

EXPERIMENTAL PROCEDURES

Metabolite Profiling

Two million HT-1080 cells were seeded in 10 cm culture dishes. The next day, cells were treated with 5 μg/ml erastin and incubated for 5 hr before metabolite extraction. A total of 4 ml of cold 80% methanol was added to the cell monolayer to extract polar metabolites using a cell scraper. The cell lysate/methanol mixture was transferred to a 15 ml tube and centrifuged at 2,000 × *g* at 4°C for 10 min to pellet debris and proteins. The supernatant was transferred to a new tube and stored at −80°C for LC-MS/MS analysis. For lipid extract preparation, 3 ml of cold 100% isopropanol was added to the cell monolayer to scrape cells. The resulting cell lysate/isopropanol mixture was transferred to a new 15 ml tube and centrifuged at 2,000 × *g* at 4°C for 10 min. The cleared supernatant was transferred to a new tube and stored at −20°C for LC-MS/MS analysis.

RSL3 Target Identification

A total of 1.5 million cells were seeded into T225 flasks (Corning) 3 days before treatment in order to be confluent on the day of treatment. Three days later, 20 flasks were washed with PBS three times to remove serum proteins from the media and then treated with either 0.5 μM (1*S*, 3*R*)-RSL3-fluorescein probe ("active probe") or 0.5 μM (1*R*, 3*R*)-RSL3-fluorescein probe ("inactive probe") in serum-free media (DMEM) for 2 hr. For the competitor-treated samples, 20 flasks of cells were treated with 0.5 μM (1*S*, 3*R*)-RSL3 ("competitor") for 20 min prior to treatment with 0.5 μM active probe for 2 hr. (The active and inactive probe-treated cells were treated with the equivalent amount of vehicle for the same time period of the competitor pretreatment.)

After treatment, the cells were washed once with PBS, trypsinized, and pelleted at 1,000 rpm. Following trypsinization, all the following steps were performed at 4°C. The pelleted cells were again washed in PBS twice to remove serum proteins added during the trypsinization. Cells were resuspended in nondenaturing lysis buffer for 20 min (50 mM HEPES, 40 mM NaCl, 2 mM EDTA, 0.5% Triton X-100, 1.5 mM Na_3VO_4, 50 mM NaF, 10 mM Na-pyrophosphate, 10 mM Na β-glycerophosphate, and Roche protease inhibitor tablet).

The resulting lysate was centrifuged at 12,000 × *g* for 15 min to pellet out insoluble materials, and the supernatant was removed. Protein concentration was determined using the Bradford assay (Bio-Rad). Subsequent pull-down and proteomics procedures are described in the Extended Experimental Procedures.

In Vivo Xenograft Mouse Study

Athymic nude mice (8 weeks; Charles River Laboratories) were injected with four million HT-1080 cells s.c. The next day, 400 μl of vehicle (0.625% DMSO/99.375% HBSS [pH 2]) or 40 mg/kg PE was delivered to the s.c. site where cancer cells were injected. Two days later, the s.c. injection was repeated. Three days later, 300 μl of vehicle or 30 mg/kg PE was administered to the mice through tail vein. Tail vein injection was repeated three more times, once every other day before the final tumor size was measured in both groups. The animal protocols containing all the procedures were approved by Columbia University's IACUC.

Statistical Analysis

All statistical analyses were performed by using Prism 6 (GraphPad Software).

SUPPLEMENTAL INFORMATION

Supplemental Information includes Extended Discussion, Extended Experimental Procedures, seven figures, one data file, and five tables and can be found with this article online at http://dx.doi.org/10.1016/j.cell.2013.12.010.

ACKNOWLEDGMENTS

We thank the Broad Institute MLPCN team and GNF for assistance in screening compounds, Alan Epstein, Riccardo Dalla-Favera, Andrew Kung, James Doroshow, and the Columbia Genome Center for providing cell lines, Siu-hong Ho for help with flow cytometry, the Columbia NYSTEM Chemical Probe Synthesis Facility (NYSTEM contract No. C026715) for synthesis of RSL3 analogs, and Dr. John Decatur and the Columbia Chemistry NMR core facility (NSF grant CHE 0840451 and NIH grant 1S10RR025431-01A1). NCI60 cell line testing and some in vivo toxicity testing were carried out through NCI/DTP. We thank Ulshulaa Dholakia and Beverly Shelton for assistance with the animal studies and Terumo Miyazawa for sharing an authentic PC-OOH standard. We thank Scott Geromanos, James Langridge, LeRoy Martin, Martha Stapels, and Johannes PC Vissers (Waters) for their support and advice on mass spectrometry data collection and analysis, and Ryan Colligan for technical assistance with mass spectrometry data processing. The cancer cell line profiling was supported by the NCI's Cancer Target Discovery and Development Network (RC2-CA148399, awarded to S.L.S.). S.L.S. is an investigator at the Howard Hughes Medical Institute. A.W.G. was supported

(F) Sensitivity profile of 53 cancer cell lines in the "NCI60" cell panel against erastin. The cell lines were grouped based on their tissue origins.

(G) The eight RCC cell lines were retested with erastin to confirm their sensitivity against erastin.

(H) Erastin and RSL3 generated lipid ROS in the two RCC cell lines.

(I) Cell death was rescued by a lipophilic antioxidant, Vit. E.

(J) GPX4 depletion by siGPX4 induced cell death in RCC cell lines. The western blot (right) confirmed expression of GPX4 protein in these RCC cell lines and knockdown of GPX4 by siRNAs. Scale bars, 30 μm.

(K) Ferroptosis inhibitors suppressed cell death induced by GPX4 knockdown but could not suppress cell death induced by the control siRNAs (siDeath) that kill cells via a nonferroptotic pathway.

Data points in (E), (G), and (I)–(K) represent mean ± SD (n = 3). $^{**}p < 0.01$; $^{***}p < 0.001$. See also Figure S7 and Table S5.

by NIH grant 5R01-CA70823-15. This research was supported by grants to B.R.S. from the US National Institutes of Health (5R01CA097061, 5R01GM085081, and R01CA161061), the Arnold and Mabel Beckman Foundation, and NYSTAR. B.R.S. is an Early Career Scientist of the Howard Hughes Medical Institute.

Received: June 10, 2013
Revised: August 30, 2013
Accepted: December 4, 2013
Published: January 16, 2014

REFERENCES

Basu, A., Bodycombe, N.E., Cheah, J.H., Price, E.V., Liu, K., Schaefer, G.I., Ebright, R.Y., Stewart, M.L., Ito, D., Wang, S., et al. (2013). An interactive resource to identify cancer genetic and lineage dependencies targeted by small molecules. Cell *154*, 1151–1161.

Brigelius-Flohé, R., and Maiorino, M. (2013). Glutathione peroxidases. Biochim. Biophys. Acta *1830*, 3289–3303.

Cotter, T.G. (2009). Apoptosis and cancer: the genesis of a research field. Nat. Rev. Cancer *9*, 501–507.

Degterev, A., Huang, Z., Boyce, M., Li, Y., Jagtap, P., Mizushima, N., Cuny, G.D., Mitchison, T.J., Moskowitz, M.A., and Yuan, J. (2005). Chemical inhibitor of nonapoptotic cell death with therapeutic potential for ischemic brain injury. Nat. Chem. Biol. *1*, 112–119.

Dixon, S.J., Lemberg, K.M., Lamprecht, M.R., Skouta, R., Zaitsev, E.M., Gleason, C.E., Patel, D.N., Bauer, A.J., Cantley, A.M., Yang, W.S., et al. (2012). Ferroptosis: an iron-dependent form of nonapoptotic cell death. Cell *149*, 1060–1072.

Dolma, S., Lessnick, S.L., Hahn, W.C., and Stockwell, B.R. (2003). Identification of genotype-selective antitumor agents using synthetic lethal chemical screening in engineered human tumor cells. Cancer Cell *3*, 285–296.

Fanélus, I., and Desrosiers, R.R. (2008). Reactive oxygen species generated by thiol-modifying phenylarsine oxide stimulate the expression of protein L-isoaspartyl methyltransferase. Biochem. Biophys. Res. Commun. *371*, 203–208.

Galluzzi, L., Vitale, I., Abrams, J.M., Alnemri, E.S., Baehrecke, E.H., Blagosklonny, M.V., Dawson, T.M., Dawson, V.L., El-Deiry, W.S., Fulda, S., et al. (2012). Molecular definitions of cell death subroutines: recommendations of the Nomenclature Committee on Cell Death 2012. Cell Death Differ. *19*, 107–120.

Hussain, S.P., Hofseth, L.J., and Harris, C.C. (2003). Radical causes of cancer. Nat. Rev. Cancer *3*, 276–285.

Irani, K., Xia, Y., Zweier, J.L., Sollott, S.J., Der, C.J., Fearon, E.R., Sundaresan, M., Finkel, T., and Goldschmidt-Clermont, P.J. (1997). Mitogenic signaling mediated by oxidants in Ras-transformed fibroblasts. Science *275*, 1649–1652.

Kakhlon, O., Gruenbaum, Y., and Cabantchik, Z.I. (2002). Repression of ferritin expression modulates cell responsiveness to H-ras-induced growth. Biochem. Soc. Trans. *30*, 777–780.

Kang, Y.J., and Enger, M.D. (1992). Buthionine sulfoximine-induced cytostasis does not correlate with glutathione depletion. Am. J. Physiol. *262*, C122–C127.

Kriska, T., and Girotti, A.W. (2005). A thin layer chromatographic method for determining the enzymatic activity of peroxidases catalyzing the two-electron reduction of lipid hydroperoxides. J. Chromatogr. B Analyt. Technol. Biomed. Life Sci. *827*, 58–64.

Kumagai, T., Matsukawa, N., Kaneko, Y., Kusumi, Y., Mitsumata, M., and Uchida, K. (2004). A lipid peroxidation-derived inflammatory mediator: identification of 4-hydroxy-2-nonenal as a potential inducer of cyclooxygenase-2 in macrophages. J. Biol. Chem. *279*, 48389–48396.

Mackinnon, A.L., and Taunton, J. (2009). Target identification by diazirine photo-cross-linking and click chemistry. Curr. Protoc. Chem. Biol. *1*, 55–73.

O'Donnell, K.A., Yu, D., Zeller, K.I., Kim, J.W., Racke, F., Thomas-Tikhonenko, A., and Dang, C.V. (2006). Activation of transferrin receptor 1 by c-Myc enhances cellular proliferation and tumorigenesis. Mol. Cell. Biol. *26*, 2373–2386.

Parthasarathy, S., Steinbrecher, U.P., Barnett, J., Witztum, J.L., and Steinberg, D. (1985). Essential role of phospholipase A2 activity in endothelial cell-induced modification of low density lipoprotein. Proc. Natl. Acad. Sci. USA *82*, 3000–3004.

Penaloza, C., Lin, L., Lockshin, R.A., and Zakeri, Z. (2006). Cell death in development: shaping the embryo. Histochem. Cell Biol. *126*, 149–158.

Ran, Q., Liang, H., Gu, M., Qi, W., Walter, C.A., Roberts, L.J., 2nd, Herman, B., Richardson, A., and Van Remmen, H. (2004). Transgenic mice overexpressing glutathione peroxidase 4 are protected against oxidative stress-induced apoptosis. J. Biol. Chem. *279*, 55137–55146.

Root, D.E., Flaherty, S.P., Kelley, B.P., and Stockwell, B.R. (2003). Biological mechanism profiling using an annotated compound library. Chem. Biol. *10*, 881–892.

Seiler, A., Schneider, M., Förster, H., Roth, S., Wirth, E.K., Culmsee, C., Plesnila, N., Kremmer, E., Rådmark, O., Wurst, W., et al. (2008). Glutathione peroxidase 4 senses and translates oxidative stress into 12/15-lipoxygenase dependent- and AIF-mediated cell death. Cell Metab. *8*, 237–248.

Sengupta, A., Lichti, U.F., Carlson, B.A., Cataisson, C., Ryscavage, A.O., Mikulec, C., Conrad, M., Fischer, S.M., Hatfield, D.L., and Yuspa, S.H. (2013). Targeted disruption of glutathione peroxidase 4 in mouse skin epithelial cells impairs postnatal hair follicle morphogenesis that is partially rescued through inhibition of COX-2. J. Invest. Dermatol. *133*, 1731–1741.

Shoemaker, R.H. (2006). The NCI60 human tumour cell line anticancer drug screen. Nat. Rev. Cancer *6*, 813–823.

Szatrowski, T.P., and Nathan, C.F. (1991). Production of large amounts of hydrogen peroxide by human tumor cells. Cancer Res. *51*, 794–798.

Trachootham, D., Zhou, Y., Zhang, H., Demizu, Y., Chen, Z., Pelicano, H., Chiao, P.J., Achanta, G., Arlinghaus, R.B., Liu, J., and Huang, P. (2006). Selective killing of oncogenically transformed cells through a ROS-mediated mechanism by beta-phenylethyl isothiocyanate. Cancer Cell *10*, 241–252.

Ueta, T., Inoue, T., Furukawa, T., Tamaki, Y., Nakagawa, Y., Imai, H., and Yanagi, Y. (2012). Glutathione peroxidase 4 is required for maturation of photoreceptor cells. J. Biol. Chem. *287*, 7675–7682.

Weïwer, M., Bittker, J.A., Lewis, T.A., Shimada, K., Yang, W.S., MacPherson, L., Dandapani, S., Palmer, M., Stockwell, B.R., Schreiber, S.L., and Munoz, B. (2012). Development of small-molecule probes that selectively kill cells induced to express mutant RAS. Bioorg. Med. Chem. Lett. *22*, 1822–1826.

Wolpaw, A.J., Shimada, K., Skouta, R., Welsch, M.E., Akavia, U.D., Pe'er, D., Shaik, F., Bulinski, J.C., and Stockwell, B.R. (2011). Modulatory profiling identifies mechanisms of small molecule-induced cell death. Proc. Natl. Acad. Sci. USA *108*, E771–E780.

Yagoda, N., von Rechenberg, M., Zaganjor, E., Bauer, A.J., Yang, W.S., Fridman, D.J., Wolpaw, A.J., Smukste, I., Peltier, J.M., Boniface, J.J., et al. (2007). RAS-RAF-MEK-dependent oxidative cell death involving voltage-dependent anion channels. Nature *447*, 864–868.

Yang, W.S., and Stockwell, B.R. (2008a). Synthetic lethal screening identifies compounds activating iron-dependent, nonapoptotic cell death in oncogenic-RAS-harboring cancer cells. Chem. Biol. *15*, 234–245.

Yang, W.S., Shimada, K., Delva, D., Patel, M., Ode, E., Skouta, R., and Stockwell, B.R. (2012). Identification of simple compounds with microtubule-binding activity that inhibit cancer cell growth with high potency. ACS Med. Chem. Lett. *3*, 35–38.

Yoo, S.E., Chen, L., Na, R., Liu, Y., Rios, C., Van Remmen, H., Richardson, A., and Ran, Q. (2012). Gpx4 ablation in adult mice results in a lethal phenotype accompanied by neuronal loss in brain. Free Radic. Biol. Med. *52*, 1820–1827.

Supplemental Information

EXTENDED DISCUSSION

Some cancer cells that originate from lymphoid tissue, including DLBCLs, are reported to have impaired cysteine metabolism due to an inability to synthesize cysteine endogenously (Iglehart et al., 1977) or due to low expression of system xc-, the cystine-glutamate antiporter (Gmunder et al., 1991). It is possible that the defective cysteine metabolism in DLBCL cell lines rendered them more sensitive to ferroptosis, as cysteine is a precursor for GSH synthesis.

We do note that some published observations are discordant with our own, such as the role of AIF downstream of *Gpx4* deletion in some models, suggesting that further examination of the short term and long term effects of *Gpx4* inhibition, knockdown and deletion in diverse contexts may be warranted.

Although iron is an essential metal required for life, it is a redox-reactive element that is tightly bound to biological ligands to prevent toxicity. We suggest two biological routes of iron-mediated lipid peroxide generation may be relevant to ferroptosis induction. One route is activation of lipoxygenases, which introduce molecular oxygen into polyunsaturated fatty acids in lipids, with regio- and stereo-selectivity (Haeggström and Funk, 2011). The catalytic site of lipoxygenases contain nonheme iron that needs to be oxidized in order to initiate the oxygenation reaction. Another source of iron-mediated lipid peroxidation is hypervalent iron generated from oxo-iron complexes found in a number of heme and nonheme iron proteins (Hohenberger et al., 2012). For example, cytochrome P450 family members catalyze oxidation of cellular metabolites and drugs using a heme-iron complex. The heme-iron complex can capture molecular oxygen to form a perferryl radical that is capable of abstracting hydrogen from unsaturated fatty acids in lipids (Mukhopadhyay and Chatterjee, 1994). Importantly, heme-iron-mediated lipid peroxidation is known to produce one enantiomer in excess, which is in contrast to achiral reactive oxygen species such as $O_2^{\bullet -}$, H_2O_2, and $\bullet OH$ (Cheng and Li, 2007). The accurate structural determination of lipid peroxides, including their stereochemical information, may clarify which specific reactive species play a major role in the initiation phase of lipid peroxidation during ferroptosis in various contexts.

As the initial hydrogen bond abstraction occurs on unsaturated fatty acids, the degree of unsaturation of membrane lipids can likely modulate cell sensitivity to ferroptosis. In this regard, lipid with long chain (13-22 carbon) or very long chain (>22 carbon) polyunsaturated fatty acids (PUFAs) should be the most efficient substrates for lipid peroxidation in biological membranes. These long chain PUFAs are synthesized by a series of reactions mediated by desaturases and elongases (Guillou et al., 2010). Studies with knock out mice for individual desaturases and elongases demonstrated loss of PUFAs by deleting *FADS1*, *FADS2*, *ELOVL2*, and *ELOVL3* genes (Guillou et al., 2010). The association of PUFAs with cancer has been controversial because the effects of changing PUFA levels are myriad; PUFAs are essential constituents of membrane structure, serve as cellular energy stores, and act as signaling molecule to control many cellular activities. However, it is established that lipid metabolism in cancer cells is often shifted toward lipogenesis to support continuous proliferation. For example, tandem activation of lipogenic enzymes such *ACL*, *AAC*, *FASN*, and *SCD1* may account for the lipogenic metabolism of cancer (Menendez and Lupu, 2007). The elevated lipid level could provide a selectivity window between normal cell and tumor cells for FIN compound sensitivity. The effect of PUFAs on ferroptosis in relation to the activity of enzymes listed above could be investigated to define cell sensitivity to FIN compounds, which may aid in stratification of patients likely to be most susceptible to FIN compounds as they move into clinical studies.

EXTENDED EXPERIMENTAL PROCEDURES

For synthesis of erastin analogs and RSL3 analogs, see Data S1.

GSH Assay

2 million cells were seeded on 10 cm dishes. The next day, cells were treated with compounds to induce GSH depletion followed by harvesting to determine cell number. Two million live cells from each sample were transferred to new tubes, and centrifuged at 1,000 rpm at 4°C for 5 min. The cell pellet was resuspended in 1 ml of PB buffer (10 mM sodium phosphate buffer, 1 mM EDTA, pH 7) and sonicated using at 60 Joule. The lysate was centrifuged at 13,200 rpm at 4°C for 10 min, and cleared lysate was used to determine the amount of GSH in the sample. We used the QuantiChrome glutathione assay kit (BioAssay Systems, cat# DIGT-250) and followed the product instructions to determine GSH levels.

Selective Lethality Testing in Four BJ Cells

In order test whether BSO and other antioxidant targeting agents exhibit the RSL phenotype, we cultured 4 BJ-derived cell lines, BJeH, BJeHLT, BJeLR, and DRD, and treated compounds in 2-fold dilution series as described (Yang and Stockwell, 2008b). Cell viability was determined using alamar blue and percent growth inhibition was computed as described (Yang and Stockwell, 2008b).

Light Microscopy

Phase contrast images were obtained using an $EVOS_{fl}$ (Advanced Microscopy Group) microscope equipped with a 10x phase-contrast objective. At least three independent fields were acquired for each experimental condition. Representative photographs from one field of view are shown.

Cellular ROS Assay Using Flow Cytometer

0.2 million cells were seeded in 6-well plates. The next day, culture media was replaced with 2 ml media containing 5 μM of CM-H_2DCF dye (Invitrogen, cat# C6827) and the culture was returned to the tissue culture incubator for 20 min. Cells were harvested in 15 ml tubes and washed twice with PBS followed by re-suspending in 500 μl of PBS. The cell suspension was filtered through cell strainer (0.4 μm nylon mesh) and subjected to the flow cytometry analysis to examine the amount of ROS within cells. C6 flow cytometry system (BD Accuri cytometers) was used for the flow cytometer analysis. When cells were prepared for flow cytometry, we observed different fluorescence intensities in the unstained samples each time, indicating that cells had different autofluorescence upon passage. In order to compensate for changes in autofluorescence, we took median fluorescence values of unstained samples and CM-H_2DCF stained samples, subtracted the latter from the former, and then, divided by the median autofluorescence. The normalized ROS level was determined in this way for BJeH, BJeHLT, and BJeLR cells on the same day. The experiment was repeated 8 times on 8 different days.

Lipid ROS level was determined using 5 μM of BODIPY-C11 dye (Invitrogen, cat# D3861) using the same approach as above.

GPX Activity Assay Using Tert-Butylhydroperoxide

48 million cells with or without compound treatment were harvested and resuspended in 300 μl of GPX assay buffer (50 mM Tris-HCl [pH 8.0], 0.5 mM EDTA). Cells were disrupted using sonication and the resulting crude lysates were cleared by centrifuging the tube at 140,000 rpm, for 10 min. The amount of protein in the cleared lysate was determined using 660nm Protein assay kit (Thermo Scientific, cat# 22662). In microtubes, GPX assay buffer, NADPH (final 0.25 mM), glutathione reductase (final 0.5 U/ml), 700 μg of cellular protein samples were transferred and mixed well. The amount of GPX assay buffer was adjusted to give the final mixture of 495 μL. GPX reaction was started by adding 5 μl of 30 mM tert-butylhydroperoxide to the mixture above. The amount of NADPH in the reaction mixture was determined kinetically by reading absorbance value at 340 nm at 10 s interval over the 5 min time.

Proteomic Sample Preparation for RSL3 Target Identification

Preclearing and Pull-Down

Anti-fluorescein beads were prepared by coupling NHS-activated Sepharose 4 Fast Flow matrix (GE Healthcare, 17-0906-01) to mouse IgG anti-FITC (Jackson Labs, 200-002-037) according to the manufacturer's instructions. For use in preclearing, "negative" beads were prepared that had the NHS reactive site blocked with ethanolamine. The anti-fluorescein bead preparations were first tested for their ability to affinity-purify a positive control protein prior to use (FITC-tagged goat anti-rabbit IgG (Jackson labs, 111-095-003)).

Protocol and buffer recipes were adapted from previously published protocols (Mackinnon and Taunton, 2009). Lysate was diluted 2-fold with "affinity purification" buffer (50 mM HEPES, 100 mM NaCl, 1% Triton X-100, pH 7.4) and first incubated with negative beads (~0.8 ml of packed beads per treatment sample) for 1 hr at 4°C on a rotator to remove nonspecific interactions with the resin. Next, the lysate was incubated with antifluorescein beads (~1.6 ml) overnight at 4°C on a rotator. The supernatant was removed the next morning and the remaining beads were washed twice in "affinity purification" buffer (beads were resuspended in buffer and rotated at 4°C for 10 min followed by centrifugation at 10,000 rpm). The beads were washed similarly in "wash" buffer (50 mM HEPES, 500 mM NaCl, 1% Triton X-100, pH 7.4) twice. The beads were eluted with 750 μl of saturated 5(6)-carboxyfluorescein in PBS (137 mM NaCl, 10 mM Na_2HPO_4, 2.7 mM KCl) for an hour at 4°C on a rotator to specifically elute fluorescein-tagged proteins; this was repeated twice more. Finally a denaturing elution was performed with 2% SDS and boiling to remove remaining bound proteins for comparison. The fluorescein elutions were combined and precipitated using standard chloroform-methanol precipitation and the final pellet was redissolved in Rapigest buffer (Waters Corp, 186001861 – prepared according to manufacturer's directions) and with 5.7 mM DTT followed by vortexing, sonification and boiling for 5 min each. The protein concentration was determined by the Bradford assay and samples were snap-frozen in liquid nitrogen and stored at −80°C until MS analysis. Three biological replicates were prepared for each treatment condition.

LC-MS/MS for RSL3 Target ID Experiment

Proteomic Sample Processing

Cysteine content in samples was reduced with dithiothreitol and alkylated with iodoacetamide, and proteins were digested with trypsin (6 ng/μl Promega Corp, #V511A in 50 mM NH4HCO3). A digest of yeast alcohol dehydrogenase (50 fmol) was added as an internal detection control. Other details of these methods were as described previously (PMC3153440).

Liquid Chromatography

Three chromatograms were recorded for each of nine biological replicates (three active, three inactive, and three competitor), yielding 27 chromatograms. Prior to analytical separation on a NanoAcquity UPLC (Waters Corp.), peptides were trapped on a Symmetry C18 Trap column, 5 μm particles, 180 mm × 20 mm (Waters Corp.), for 2 min at 10 μL/minute in 1% solvent B (0.1% formic acid in acetonitrile)/99% solvent A (0.1% formic acid, aqueous). Analytical separation was performed in a 120 min chromatogram on a 75 μm ID x 25 cm HSS T3 1.8 μm particle diameter reverse phase C18 column at a flow rate of 300 nL/min with an acetonitrile/formic acid gradient held at 45°C. For the analytical separation, Solvent B was increased in a 90 min linear gradient between 5 and 40% and postgradient cycled to 95% B for 7 min, followed by postrun equilibration at 5% B.

Mass Spectrometry

Identification and quantitation of proteins was performed by label-free shotgun proteomic profiling using data-independent scanning (MS^E) (Silva et al., 2006). Spectra were recorded on a Synapt G2 HDMS (quadrupole-time-of-flight) mass spectrometer (Waters Corp) in positive ion, resolution mode with ion mobility activated. Source settings included extraction cone at 2 V, sampling cone at 30 V, and source temperature 80°C. Collision energy in the trap was held at 4 eV for a low energy scan and ramped in the transfer cell from 27-50 eV for the high energy scan with a collision gas flow (Ar) of 2.5 ml/minute in the trap region. Nitrogen gas flow into the ion mobility spectrometry (IMS) cell was 90 ml/min and the helium gas flow into the helium cell (at the entry to the IMS cell) was 180 ml/min. A reference sprayer was operated at 300 nL/minute to produce a lockmass spectrum with Glu-1-Fibrinopeptide B (m/z 785.8426) every 30 s.

Data Analysis

Spectra were analyzed with ProteinLynx Global Server (PLGS) (version 2.4 RC7) (Waters Corp.) for MS^E data and with PLGS version 2.5 RC9 for MS^E–IMS data. The data were searched against a database of human protein sequences (reviewed canonical sequences with isoforms) from UniProt release 2011_04 (April 5, 2011). The database also contained sequences for yeast alcohol dehydrogenase, porcine trypsin, bovine serum proteins (BSA, serotransferrin, fibrinogen alpha chain, fibrinogen beta chain and fibrinogen gamma-B). This database was comprised of 35,353 protein sequences (20,652,583 amino acid residues). Data mining and statistical analysis was performed with TransOmics informatics for Proteomics (TOIP) (V. 1.1.4832) (Waters Corporation). p values for differential expression were calculated with false discovery rate (FDR) correction for multiple testing applied to the means of each biological replicate (Benjamini and Hochberg, 1995). In addition to p values, separate peptide counts indicated the number of peptides supporting identification and quantitation. A peptide score also indicated the mean quality of peptide identifications.

Proteomics

Proteins identified and quantified are listed in Table S2. Relative intensities (amounts) of each protein in each LC/MS/MS chromatogram are given in the body of the table. Each protein identification is supported by two or more peptides. Table S2 summarizes mean sequence coverage (%), mean precursor and product RMS errors (ppm) for all 27 chromatograms as measured by the PLGS software. For TransOmics processing, only proteins with a peptides score greater than 4.0 were included in the analysis. Additional filters in TransOmics applied to the final data increased the stringency of accepted protein leads by limiting the number of peptides used for quantitation to ≥ 2, the ratio between abundance of active protein compared to controls ≥ 2, and $p < 0.01$ for all comparisons. A preliminary set of analyses was performed on the same samples using positive ion, resolution mode but without ion mobility activated (data not shown but raw data will be submitted to an international repository). Consideration of all top hits from these two analyses generated the five top protein candidates. As indicated in the main body of the paper RNAi-mediated silencing of mRNAs encoding those five proteins revealed that knockdowns of GPX4 sensitized cells to (1*S*, 3*R*)-RSL3. Example data supporting identification of GPX4 protein by mass spectrometry is provided (Figure S3A). All raw mass spectrometry data are being deposited in an international online repository (Chorus) at http://chorusproject.org/.

Western Blotting to Confirm RLS3 Binding to GPX4

Lysates were prepared as described above in Lysate preparation. After quantification by Bradford, samples were mixed with 5X SDS loading buffer and separated by SDS-polyacrylamide gel electrophoresis. Western transfer was performed using the iBlot system (Invitrogen). Membranes were blocked for 10 min in Tris-buffered saline (pH 7.4) with 1% Tween-20 (TBS-T) with 5% milk and incubated in primary antibody overnight at 4°C. Following 3X for 5 min washes in TBS-T, the membrane was incubated with secondary antibodies for 1 hr. The membrane was washed again in TBST 3X for 5 min prior to visualization using enhanced chemiluminescence (SuperSignal West Pico Substrate, Pierce). Antibodies for GPX4 (R&D systems, MAB5457; Abcam, ab41787) were used at 1:100 or 1:1000 dilution respectively, and detected using a goat α mouse HRP conjugate secondary antibody (Santa Cruz, sc-2030) at 1:5000 dilution.

GPX4 Activity Assay Using HP-TLC

COH BR1 (L7G4 variant) cells were grown in DME/F12 media (Invitrogen 11330-032) with 10% FBS, 1% Pen/Strep, 10 ng/ml of sodium selenite and 0.5 mg/ml geneticin. Cells were treated with compound at the indicated concentration in media for 1.5 hr and then harvested by trypsinization and pelleted by centrifugation. Cells were re-suspended in lysis buffer (Chelexed PBS (25 mM sodium phosphate/125 mM NaCl [pH 7.4]) with 1.0 mM EDTA, 0.1 mM DFO, 25 μM BHT, 0.3% Triton X-100, 1X protease inhibitor) and pelleted at 12,000 rpm at 4°C for 15 min. Supernatant was removed for use in the assay (stored at −20°C). Protein concentration was determined by the Bradford assay. Reaction mixtures (105 μL) contained 150 μg of cell lysate, 5 mM GSH, in Chelexed PBS containing 50 μM DFO, 1 mM EDTA and 100 μM 7α cholesterol hydroperoxide (added last to initiate reaction) and were incubated at 37°C. Peroxides were extracted at indicated time points by removing 30 μl of the reaction and adding 30 μl of ice cold chloroform:methanol (6:3), vortexing for 1 min and centrifugation at 4,000 rpm. The upper aqueous layer and protein at the interface was discarded and the solvent was evaporated under a stream of N_2 gas and stored at −20°C until HPTLC analysis. The HPTLC plate was preheated for 1 hr at 110°C (Analtech HPTLC Uniplates, Sigma, Z265292) and allowed to cool. The dried peroxides were dissolved in 10 μl of hexane:ethanol (4:1) and applied to the plate with a TLC spotter (calibrated micropipets from Drummond) to keep the spot size as small as possible. Chromatography was carried out using benzene/ethyl acetate (1:1) as the mobile phase. The plate was dried under a stream of N_2 and then sprayed with a fine mist of N,N,N′,N′-tetramethyl-p-phenylenediamine (1% w/v) in methanol/water/acetic acid (50:50:1) and dried under a stream of N_2. The plate was clamped to a glass plate to minimize exposure to air and allowed to develop for 15 min. Analytes were scanned and quantified using ImageJ. The plate was sprayed with H_2SO_4 using a TLC reagent sprayer (VWR, KT422530-0050) and heated in the oven at 110°C for 15 min to visualize the corresponding alcohol product.

Lentiviral shRNA Production

Viral shRNA plasmids were derived from bacterial glycerol stocks of The RNAi Consortium (TRC) collection. Virus production followed the protocol of TRC. For production of virus, 293-T cells were seeded in 6-well dishes in antibiotic free media (280,000 cells/well). The next day, cells were transfected using FuGENE with shRNA encoding plasmid (450 ng), viral packaging plasmid (p-Delta8.9, 400 ng), and viral envelope plasmid (p-VSV-G, 45 ng). After 24 hr, media was removed and replaced with 2 ml Viral Collection Media. A total of 3 collections of viral supernatant in VCM per shRNA were made over 36 hr and pooled. Pooled supernatant was centrifuged (2,250 rpm, 2 min), aliquoted and stored at −80°C.

Lentiviral shRNA Infection

For lentiviral infections in 384-well format, 400 cells were seeded per well the night before the infection. On the day of the infection, media was replaced with 38 μl media + polybrene (8 μg/ml) and 2 μl of the viral supernatant per well. Plates were centrifuged at 2,250 rpm at 37°C for 90 min in a tabletop Sorvall centrifuge. Plates were incubated for 48 hr, the media was replaced with media containing 1.5 μg/ml puromycin and incubated for 24 hr at 37°C using Biomek FX. Stock solutions of (1S, 3R)-RSL3 in DMSO were diluted into media to 1X final highest test concentration of treatment and a 2-fold dilution series of each was prepared using a multichannel pipette. Cell medium was replaced with 40 μl of RSL3 or compound containing media. Plates were incubated for 24 hr and viability was assessed using Alamar Blue. For lentiviral infections in 6-well format, 35,000 cells were seeded per well in 2 ml of media the night before the infection. Cells were infected in the presence of 8 μg/ml polybrene in 1.85 ml of media with 150 μl viral supernatant. Puromycin selection, compound treatment was the same as above, but scaled for 6-well format. Cells were harvested and viability was assessed by Trypan Blue exclusion.

siRNA Transfection

Small interfering RNA (siRNA) SMARTpools targeting each gene and siNeg were obtained from Dharmacon Technologies. Reverse transfection was performed by preparing a solution of 1 ml of Opti-MEM (Invitrogen), 6 μl of lipo-RNAiMAX (Invitrogen) and 2 μl of siRNA solution (at 1,000X desired concentration) and incubating the mixture (1 ml/well) in a 6-well dish for 20 min at 37°C. Following incubation, 200,000 cells suspended in 1 ml of 2X serum-containing media were transferred to each well and incubated for 48 hr. For viability measurements two days later, cells were trypsinized and reverse transfected again. Viability was assessed by Trypan Blue exclusion. For drug treatment experiments, cells were reseeded after two reverse transfections into 384-well format and dose response curves were performed as described above.

Gene Expression Analysis by RT-qPCR

Cells from 6-well format lentiviral shRNA infection were harvested following puromycin selection and RNA was purified using the QIAshredder and RNAeasy extraction kits (QIAGEN) according to the manufacturer's instructions. 2 μg total RNA per sample was subsequently used in a reverse transcription reaction using the TaqMan RT Kit priming with Random Hexamers (Applied Biosystems). Primers for qPCR were designed with Primer Express. Quantitative PCR was performed on triplicate samples in 96-well format using Power SYBR Green Master Mix (Applied Biosystems) on an Applied Biosystems 7300 Cycler set to absolute quantification. The change in expression of a gene between experimental and control conditions was computed using the ΔΔCt method with ACTB as an internal reference gene.

Generating Stable Cell Lines Expressing GPX4-Cyto and GFP-GPX4-Cyto

A cDNA of GPX4 (GeneBank ID: NM_002085.3) was cloned into a pBabe-puro vector to express cytosolic GPX4 (GPX4-cyto) in cells. The plasmid (or the original vector as a control) was transfected into PLAT-GP cells (Cell Biolabs, cat# RV-103) along with pVSV-G helper plasmid to produce retrovirus harboring the expression plasmid. HT-1080 cells were seeded into a six well dish at a density of 8,000 cells/well the night before infection. Cells were infected as described above in "Lentiviral shRNA infection" in the presence of 8 μg/ml polybrene in 1.33 ml with 667 μl viral supernatant. Following infection, cells were passaged several times in media containing 1.5 μg/ml puromycin and grown in this media for all experiments performed.

GFP-GPX4-cyto expression vector was constructed using the same strategy above except GFP cDNA was fused at the N-terminal of GPX4-cyto cDNA.

GPX4 Activity Assay Using LC-MS

Phosphatidyl choline hydroperoxide (PC-OOH) was prepared using lipoxygenase enzyme as described previously (Roveri et al., 1994). Cell lysates with or without compound treatment were prepared as described (Kriska et al., 2008). In a typical assay mixture, 10 μl of PC-OOH, 200 μg of cell lysates and 5 mM of GSH were added to a microtube, and the total volume was increased to 500 μl using GPX4 reaction buffer (final buffer concentration of 25 mM sodium phosphate, 125 mMNaCl, 1 mM EDTA, 0.1 mM DFO, 0.1%

peroxide free Triton X-100; pH 8.0). The reaction mixture was vortex-mixed and incubated at 37°C for 10 min followed by lipid extraction using chloroform:methanol = 2: 1 (v/v) solution. The lipid extract was dried and reconstituted with 100% methanol before injecting into LC-MS instrument.

LC-MS analyses were carried out on Ultimate 3000 RSLC (Thermo scientific) coupled to amaZon SL ion trap mass spectrometer (Bruker). The reconstituted lipid extract was separated on Zorbax eclipse plus C18 column(2.1 × 50 mm; 1.8 μm particle size) that was maintained at 40°C. The mobile phase consisted of 10 mM ammonium acetate: methanol: acetic acid (95:5:0.1, solvent A) and 0.1% acetic acid in ml/min. The total run time was 15 min. The HPLC eluent was introduced to amaZon ion trap by electrospray interface. The instrument was operated under Ultrascan mode with positive ion selectivity. The mass range between m/z 500 and 900 was recorded during the acquisition and EIC m/z of 790.6 $[M+H]^+$was analyzed to determine the amount of PC-OOH in the sample. Authentic standard of PC-OOH was obtained from Dr. Miyazawa (Ibusuki et al., 2008) and used to validate LC-MS based assays.

Metabolic Stability Test

The mouse liver microsome assay on erastin and PE was performed at Shanghai Medicilon Inc.

In Vivo Xenograft Mouse Study

In the prevention study with (1*S*, 3*R*)-RSL3, athymic nude mice (8 weeks, Charles River) were injected with 4 million BJeLR cells subcutaneously (SC). The next day, 400 μl of vehicle (PEG-400) or 100 mg/kg (1*S*, 3*R*)-RSL3 were delivered to the SC site where cells were injected. Three weeks later the final tumor size was measured in both groups. In the therapeutic study, mice xenografts were allowed to grow for 1 week prior to injection with 100 mg/kg (1*S*, 3*R*)-RSL3 intratumorally twice per week for 2 weeks. Tumor size was measured 4 weeks after cell injection.

The animal protocols containing all the procedures were approved from Columbia University's IACUC.

Ptgs2 Expression Analysis from Mouse Tissues

Mice were euthanized using CO_2 gas chamber before harvesting liver and tumor tissues. The dissected tissues were cut into smaller pieces with a size of 100 mg, snap frozen by immersing into liquid nitrogen, and stored at −80 degree until the day of mRNA preparation. The frozen tissues were homogenized with FastPrep instrument (MP Biomedicals), and the total mRNA was prepared from the cleared homogenate using Ribopure kit (Life Technologies), and was reverse-transcribed using a High Capacity cDNA Reverse Transcription kit (Life Technologies). The resulting cDNA samples were mixed with TaqMan® probes for Ptgs2 gene, and arrayed on 96-well plate in triplicates. The plate was loaded onto ViiA7 Real-Time PCR system (Life Technologies) for qPCR. Comparative analysis (delta delta Ct analysis) was performed using Actb (mouse actin b) Ct value as a control.

Cell Lines

The 4 BJ-derived cell lines, HT-1080 cells, and U-2-OS cells were maintained as described previously (Yang and Stockwell, 2008b). Renal cell carcinoma cell lines, A498, TK-10, SN12C, CAKI-1, RXF-393, ACHN, 786-0, and UO-31, were purchased from NCI, and cultured using RPMI1640/10% fetal bovine serum media. NU-DUL-1, SU-DHL-1, −7, −8, and −9 were from Dr. Alan Epstein (University of Southern California). WSU-DLCL2 cells were from Dr. Riccardo Dalla-Favera at Columbia University. All the other cell lines were obtained from Columbia Genome Center.

Software

FlowJo (9.5.2, Tree Star, Inc.) was used to analyze Flow cytometry data. Chemical structures were drawn using ChemDraw Ultra (10.0, Cambridgesoft). The heatmap in the modulatory profiling was generated using R programming language. Dose-response curves were generated in Prism 6 (GraphPad Software). Images were manipulated using ImageJ (1.41o, NIH), PhotoshopCS4 and Illustrator CS4 (Adobe).

SUPPLEMENTAL REFERENCES

Benjamini, Y., and Hochberg, Y. (1995). Controlling the false discovery rate—a practical and powerful approach to multiple testing. J. R. Stat. Soc. Series B Stat. Methodol. *57*, 289–300.

Cheng, Z., and Li, Y. (2007). What is responsible for the initiating chemistry of iron-mediated lipid peroxidation: an update. Chem. Rev. *107*, 748–766.

Gmunder, H., Eck, H.P., and Dröge, W. (1991). Low membrane transport activity for cystine in resting and mitogenically stimulated human lymphocyte preparations and human T cell clones. Eur. J. Biochem. *201*, 113–117.

Guillou, H., Zadravec, D., Martin, P.G., and Jacobsson, A. (2010). The key roles of elongases and desaturases in mammalian fatty acid metabolism: insights from transgenic mice. Prog. Lipid Res. *49*, 186–199.

Haeggström, J.Z., and Funk, C.D. (2011). Lipoxygenase and leukotriene pathways: biochemistry, biology, and roles in disease. Chem. Rev. *111*, 5866–5898.

Hohenberger, J., Ray, K., and Meyer, K. (2012). The biology and chemistry of high-valent iron-oxo and iron-nitrido complexes. Nat. Commun. *3*, 720.

Ibusuki, D., Nakagawa, K., Asai, A., Oikawa, S., Masuda, Y., Suzuki, T., and Miyazawa, T. (2008). Preparation of pure lipid hydroperoxides. J. Lipid Res. *49*, 2668–2677.

Iglehart, J.K., York, R.M., Modest, A.P., Lazarus, H., and Livingston, D.M. (1977). Cystine requirement of continuous human lymphoid cell lines of normal and leukemic origin. J. Biol. Chem. *252*, 7184–7191.

Kriska, T., Levchenko, V.V., Chu, F.F., Esworthy, R.S., and Girotti, A.W. (2008). Novel enrichment of tumor cell transfectants expressing high levels of type 4 glutathione peroxidase using 7alpha-hydroperoxycholesterol as a selection agent. Free Radic. Biol. Med. *45*, 700–707.

Menendez, J.A., and Lupu, R. (2007). Fatty acid synthase and the lipogenic phenotype in cancer pathogenesis. Nat. Rev. Cancer *7*, 763–777.

Mukhopadhyay, C.K., and Chatterjee, I.B. (1994). NADPH-initiated cytochrome P450-mediated free metal ion-independent oxidative damage of microsomal proteins. Exclusive prevention by ascorbic acid. J. Biol. Chem. *269*, 13390–13397.

Roberts, L.D., Souza, A.L., Gerszten, R.E., and Clish, C.B. (2012). Targeted metabolomics. Curr. Protoc. Mol. Biol. *Chapter 30*, Unit 30.2.1–30.2.24.

Roveri, A., Maiorino, M., and Ursini, F. (1994). Enzymatic and immunological measurements of soluble and membrane-bound phospholipid-hydroperoxide glutathione peroxidase. Methods Enzymol. *233*, 202–212.

Silva, J.C., Denny, R., Dorschel, C., Gorenstein, M.V., Li, G.Z., Richardson, K., Wall, D., and Geromanos, S.J. (2006). Simultaneous qualitative and quantitative analysis of the *Escherichia coli* proteome: a sweet tale. Mol. Cell. Proteomics *5*, 589–607.

Yang, W.S., and Stockwell, B.R. (2008b). Inhibition of casein kinase 1-epsilon induces cancer-cell-selective, PERIOD2-dependent growth arrest. Genome Biol. *9*, R92.

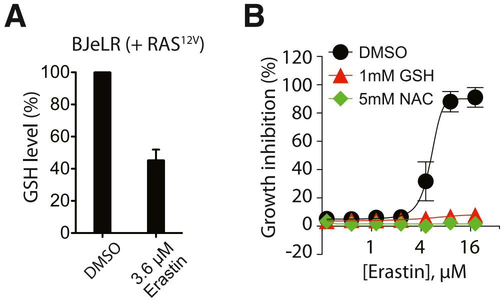

Figure S1. GSH Depletion Is a Functionally Important Biochemical Change in Erastin-Induced Ferroptosis, Related to Figure 1

(A) BJeLR cells were treated with 3.6 μM erastin or vehicle (DMSO) for 24 hr. The cellular GSH level in each sample was determined as described in the Extended Experimental Procedures.

(B) Supplementation of the culture medium with 1 mM GSH or 5 mM N-acetylcysteine (NAC), a GSH biosynthetic precursor, prevented erastin lethality in U-2 OS cells. Cell viability was determined using alamar blue after 24 hr. Data are presented as mean ± SD; n = 3.

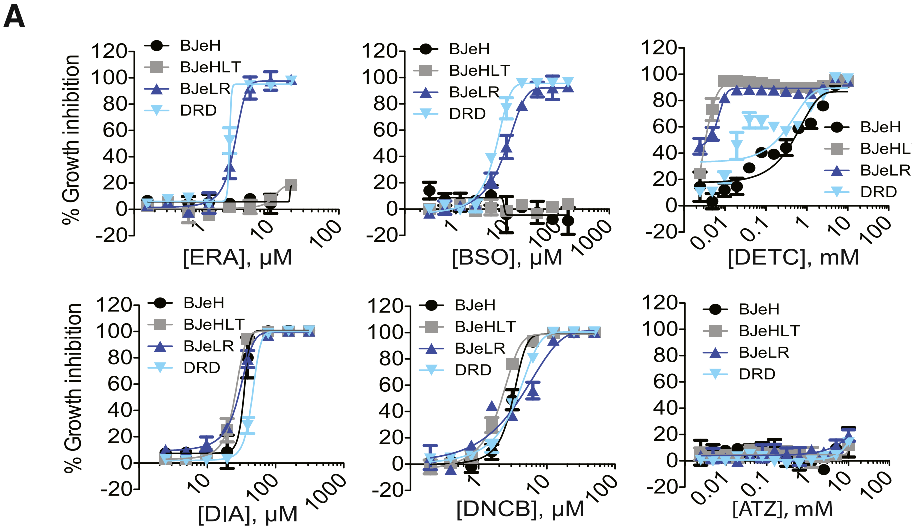

B

Abbr.	Full name	Target	Biological consequences
ERA	erastin	VDACs, system x_c^-	Depletes GSH
BSO	Buthionine sulfoximine	GCLC	Prevents GSH synthesis
DETC	Sodium diethyldithiocarbamate trihydrate	SOD	Inhibits superoxide dismutase
DNCB	1-Chloro-2,4-dinitrobenzene	TrxRs	Inhibits thioredoxin reductase irreversibly
DIA	Diamide	Cellular thiols	Reactive to cellular thiols including GSH
ATZ	3-Amino-1,2,4-triazole	Catalase	Inhibition of catalase

Figure S2. Testing of Compounds Targeting Cellular Antioxidant Systems in the Four BJ-Derived Cell Lines, Related to Figure 2

(A) Dose-response curves for growth inhibition by antioxidant inhibitors in 4 BJ-derived cell lines. Cells were treated with each compound for 24 hr.

(B) The table lists the compounds used in the 4 BJ-derived cell line testing with the target information. Data are presented as mean ± SD; n = 3.

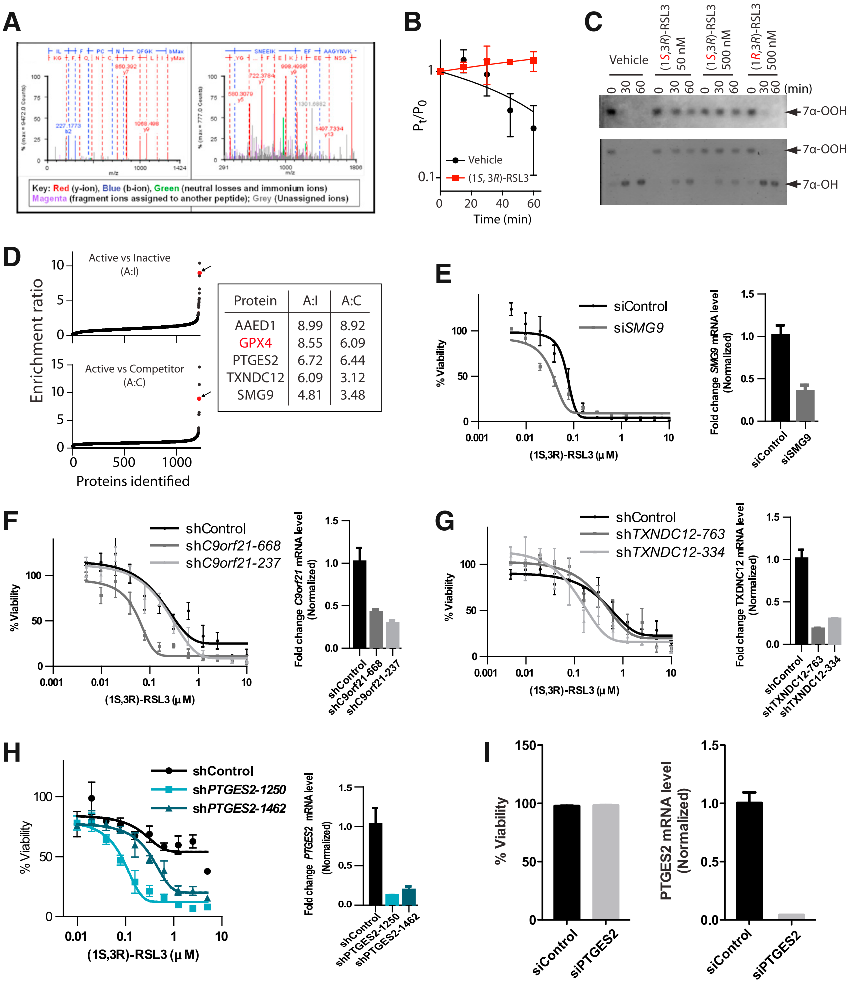

Figure S3. (1*S*, 3*R*)-RSL3 Binds to and Inhibits GPX4, Related to Figure 3

(A) GPX4 was identified by MS^E-IMS mass spectrometry as enriched in affinity pull-downs prepared from lysates treated with (1*S*, 3*R*)-RSL3-fluorescein probe. Fragmentation (high-energy MS/MS) spectra are shown for two example peptides (left: ILAFPCNQFGK 1294.66 M+H and right: QEPGSNEEIKEFAAGYNVK 2110.02 M+H) from GPX4 recorded in MS^E-IMS mode providing evidence supporting the peptide and protein identification.

(B) HPTLC-based GPX4 assay confirmed GPX4 inhibition by (1*S*, 3*R*)-RSL3. First-order plot depicting the time course of 7α-cholesterol hydroperoxide (7α-OOH) loss for L7G4 cells treated with 50 nM (1*S*,3*R*)-RSL3 or vehicle measured in Figure 3I. Densitometrically determined 7α-OOH at time-zero and time-t is denoted by P_0 and P_t, respectively. Data points are means from duplicate experiments.

(C) GPX4-catalyzed reduction of 7α cholesterol hydroperoxide (7α-OOH) to the corresponding alcohol (7α-OH) in cell lysates treated with (1*S*, 3*R*)-RSL3 (50 or 500 nM), (1*R*, 3*R*)-RSL3 (500 nM) or vehicle was monitored by high performance thin layer chromatography (HPTLC). HPTLC plates were visualized with tetramethylphenylenediamine solution (above) or sulfuric acid (below) (see Extended Experimental Procedures).

(D) Schematic of the selection process of top candidate targets of (1*S*, 3*R*)-RSL3 from an affinity-based chemoproteomic experiment. The chemoproteomics data were preliminarily analyzed with Elucidator software (Rosetta Biosoftware). Proteins (listed along x axes) were selected on the basis of exhibiting greater than 3-fold enrichment in both active:inactive (A:I) and active:competitor (A:C) probe treatments, along with detection in two independent proteomic analyses of the samples. These selection criteria yielded five top candidate hits: GPX4 (glutathione peroxidase 4), PTGES2 (prostaglandin E synthase 2), TXNDC12 (thioredoxin domain containing 12), SMG9 (smg-9 homolog [*C. elegans*]) and AAED1(AhpC/TSA antioxidant enzyme domain containing 1). Mean values for A:I and A:C from both proteomic analyses are shown.

(E–H) Viability of HT-1080 cells infected with shRNAs targeting *SMG9*, *C9ORF21*, *TXNDC12* or *PTGES2* for 72 hr and treated with (1*S*, 3*R*)-RSL3 for 24 hr was assessed using Alamar Blue. Note that infection with viral shRNAs in general caused resistance to RSL3 and other compounds, and thus a rightward shift in potency from parental cells. Data represent mean ± SD from one of three experiments. mRNA levels for target genes upon shRNA treatment were determined using RT-qPCR (right side of each plot). Comparative analysis was carried out using *ACTB* (human actin B) gene as an endogenous control.

(I) Given that knockdown of *PTGES2* caused some sensitization to RSL3, we used siRNAs to achieve a more complete knockdown of *PTGES2* to test whether it was essential for cell viability. HT1080 cells were transfected with a pool of siRNAs targeting *PTGES2* (20 nM) or a nontargeting control (20 nM) and viability assessed with Trypan blue. Data represent mean ± SD from one of two experiments. mRNA levels were determined using RT-qPCR. Knockdown of *PTGES2* did not cause lethality, suggesting it is not relevant to the death mechanism. Knockdown of *PTGES2* and *GPX4* together did not result in any enhanced cell death beyond knockdown of *GPX4* alone (data not shown).

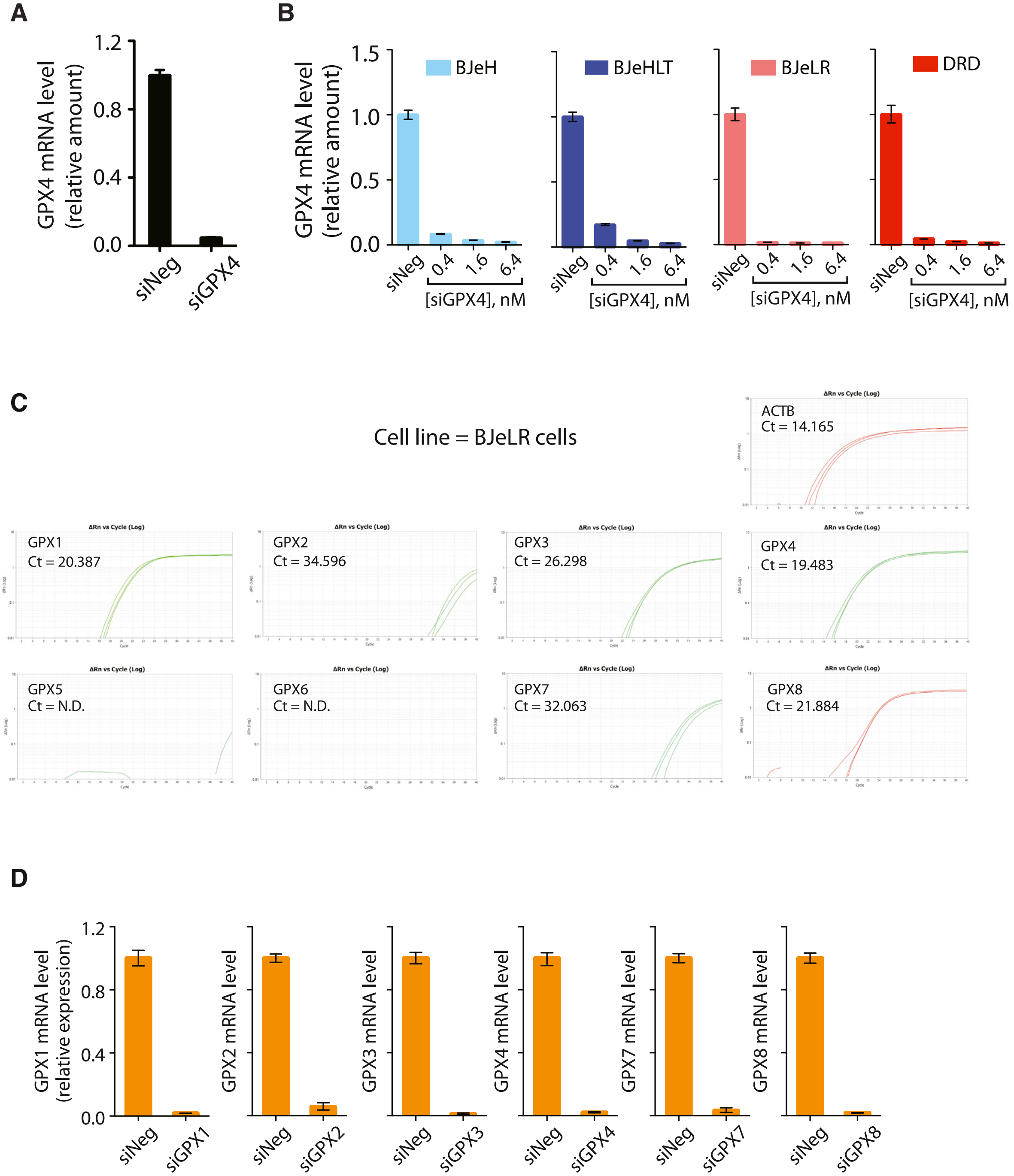

Figure S4. Confirmation of GPX Knockdowns by siRNAs Specific to Each Isoform, Related to Figure 4

(A) HT-1080 cells were transfected with 6.4 nM siGPX4 for 4 days. Reduction of GPX4 expression was confirmed by qPCR.

(B) Knockdown of GPX4 expression by the siRNA pool was confirmed using qPCR analysis in 4 BJ cell lines. Comparative analysis was carried out using ACTB (human actin B) gene as an endogenous control. Data are presented as mean ± SD; n = 3.

(C) The expression of each GPX isoform in BJeLR cells was examined by qPCR. Amplification plot of each GPX isoform is shown. Triplicate samples were analyzed for each mRNA in BJeLR cells. ACTB gene amplification was also monitored as a technical control. The gene name and the Ct (cycle of threshold) number are shown. N.D. = not determined.

(D) Knockdown of each GPX isoform by individual siRNA pools was confirmed by qPCR analysis. Data are presented as mean ± SD; n = 3.

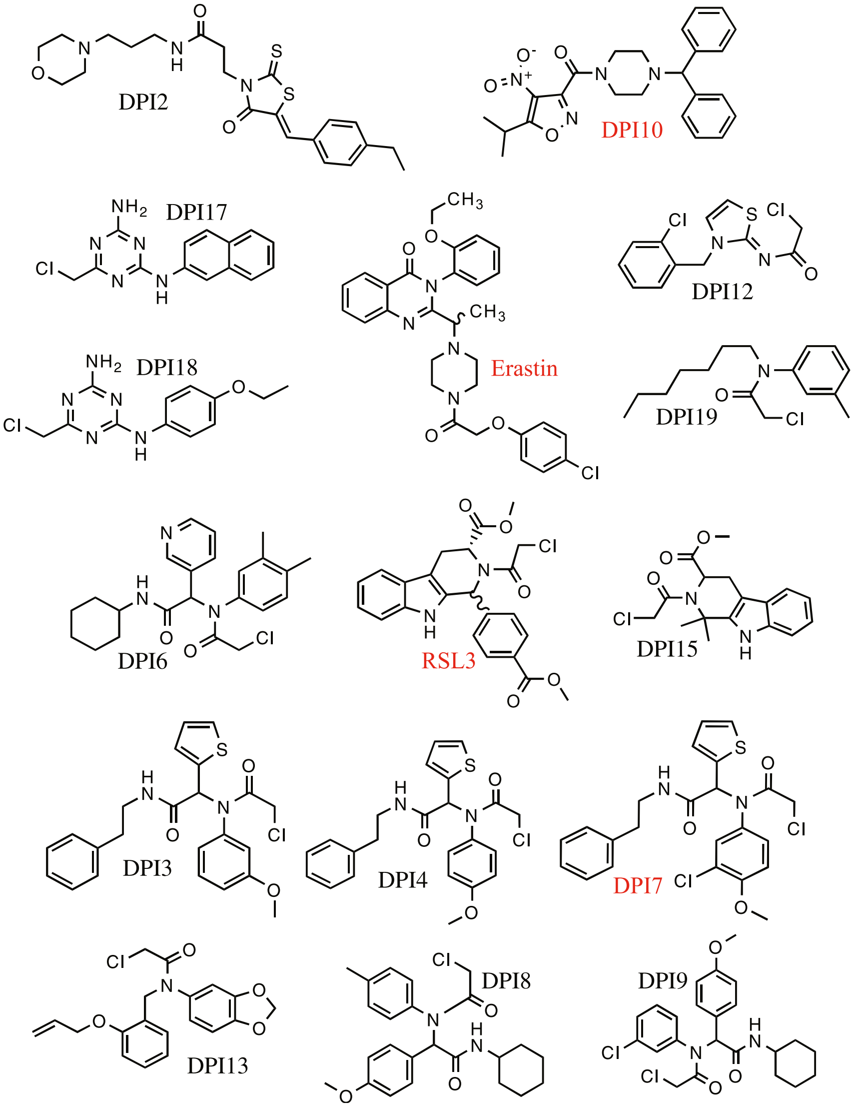

Figure S5. Structure of FIN Compounds Discovered from a High-Throughput Screening Campaign, Related to Figure 5

80,497 compounds were purchased or synthesized, 303,282 compounds were obtained through the MLPCN and 658,301 compounds in collaboration with the Genomics Institute of the Novartis Research Foundation (GNF). Structures of erastin, RSL3, DPI7, and DPI10 have been published and are marked in red.

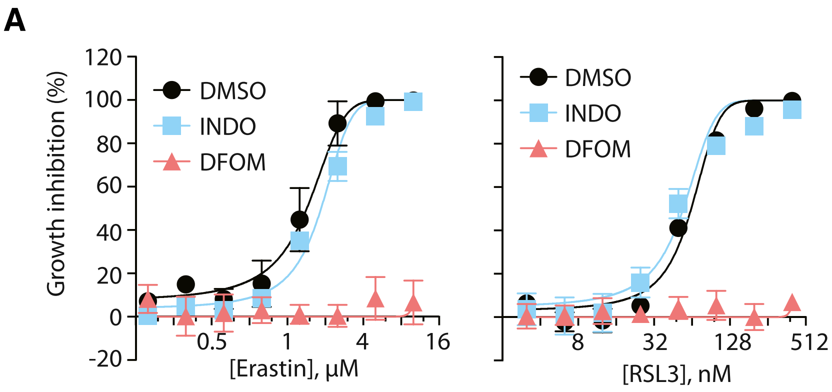

B

Nontumored Animal Toxicity Assay for (1*S*, 3*R*)-RSL3

Report generated on 09-Aug-2012

EXPERIMENT: AAZ-647 / 0 / 8B	**TUMOR: NO CELLS**	**HOST: Athymic Nudes**
MEMO NO:	**SOURCE/LINE: 0**	**SOURCE: APA**
BOOK NO:	**IMPLANT SITE: 0**	**SEX: F**

	TREATMENT					
Grp	**NSC**	**Dose/Units**	**Rt.**	**Schedule**	**Death Days**	**Surv/Total Day 14**
7	**(1*S*,3*R*)-RSL3**	100.00 mg/kg/dose	IP	QD X 1, Day 0	--	1/1
8	**(1*S*,3*R*)-RSL3**	200.00 mg/kg/dose	IP	QD X 1, Day 0	--	1/1
9	**(1*S*,3*R*)-RSL3**	400.00 mg/kg/dose	IP	QD X 1, Day 0	--	1/1

VEHICLES

Grp 7 ->	**(1*S*,3*R*)-RSL3** / 2 (Dose = 100.00)	: in 100% DMSO	(Soluble - no visible particles)	200.0 mg/ml	Inj. Vol.: 0.5 ul/gm body wt
Grp 8 ->	**(1*S*,3*R*)-RSL3** / 2 (Dose = 200.00)	: in 100% DMSO	(Soluble - no visible particles)	200.0 mg/ml	Inj. Vol.: 1 ul/gm body wt
Grp 9 ->	**(1*S*,3*R*)-RSL3** / 2 (Dose = 400.00)	: in 100% DMSO	(Soluble - no visible particles)	200.0 mg/ml	Inj. Vol.: 2 ul/gm body wt

NOTE: All treatment was administered according to exact body weight.

Figure S6. Animal Study of Two Ferroptosis Inducers, PE and (1*S*, 3*R*)-RSL3, Related to Figure 6

(A) Inhibition of the PTGS2 (COX-2) enzyme, a ferroptosis marker, did not suppress ferroptotic cell death by erastin and RSL3. BJeLR cells were treated with indicated concentration of erastin or RSL3 in the presence of vehicle (DMSO), 200 μM of indomethacin (INDO; COX-1 and −2 inhibitor), or 100 μM of deferoxamine (DFOM; iron chelator). One day after the treatment, cell viability at each condition was determined using alamar blue, a fluorescent viability dye. Percent growth inhibition was calculated using the fluorescence values of alamar blue. Data points represent mean ± one SD.

(B) In vivo toxicity assessment for intraperitoneal injection of (1*S*, 3*R*)-RSL3. (1*S*, 3*R*)-RSL3 was delivered intraperitoneally to female athymic nude mice at 100 mg/kg, 200 mg/kg, or 400 mg/kg dose, and its toxicity was monitored for 14 days.

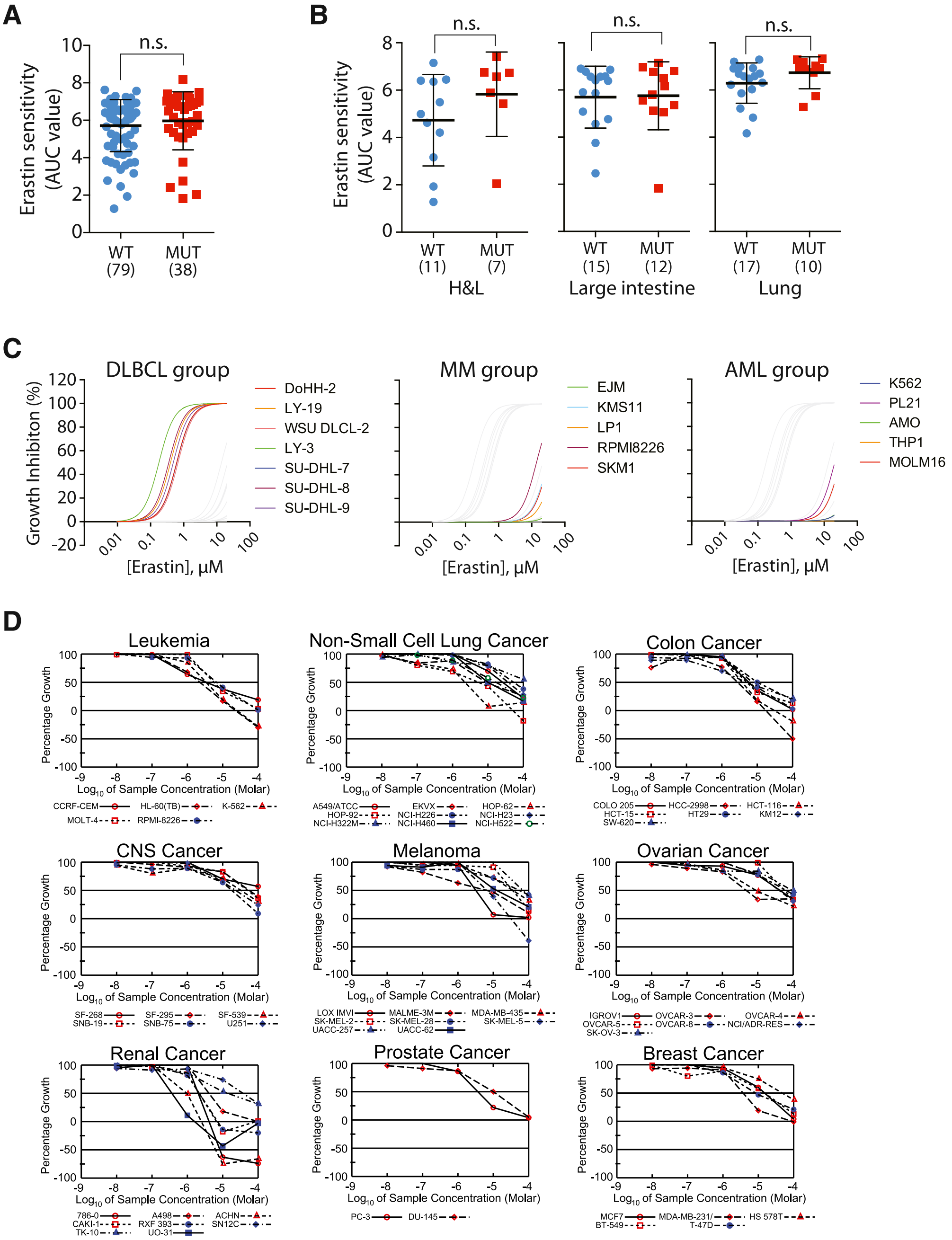

Figure S7. DLBCLs and RCCs Are Sensitive to Ferroptosis, Related to Figure 7

(A) RAS mutation status did not predict cell line sensitivity to erastin. There was no statistically significant difference in erastin's sensitivity between 79 RAS wild-type cancer cells and 38 RAS mutated cancer cells. The cancer cells were derived from hematopoietic and lymphoid (H&L), large intestine, ovarian, lung, and skin tissue lineages.

(B) RAS selective lethality of erastin did not manifest even in single-lineage analyses. Note that skin and ovarian tissues were excluded from the analysis, as the number of RAS-mutated cell lines was too small ($n < 4$). The data were presented as mean ± SD. Sample number was presented in the parenthesis. n.s. = not significant.

(C) Concentration-dependent growth inhibition curve of erastin in individual cell lines tested in Figure 7B. Each cell line was treated with erastin in a 2-fold dilution series manner in six replicates. The growth inhibition curves were fitted with nonlinear regression method using Prism 6 (GraphPad software). DLBCL = Diffuse large B cell lymphoma, MM = Multiple myeloma, AML = Acute myeloid leukemia.

(D) Concentration-response curves of erastin in NCI60 cancer cell lines. Sample = Erastin.